THE GEOLOGICAL SOCIETY OF AMERICA®

The origin and evolution of breakouts in a cooling-limited rhyolite lava flow

Nathan Magnall[1,†], Mike R. James[1], Hugh Tuffen[1], Charlotte Vye-Brown[2], C. Ian Schipper[3], Jonathan M. Castro[4], and Ashley Gerard Davies[5]

[1]*Lancaster Environment Centre, Lancaster University, Lancaster LA1 4YQ, UK*
[2]*The Lyell Centre, British Geological Survey, Edinburgh EH14 4AP, UK*
[3]*School of Geography, Environment and Earth Sciences, Victoria University of Wellington, PO Box 600, Wellington 6140, New Zealand*
[4]*Institute of Geosciences, University of Mainz, Becherweg 21, Mainz D-55099, Germany*
[5]*Jet Propulsion Laboratory, California Institute of Technology, 4800 Oak Grove Drive, Pasadena, California 91109, USA*

ABSTRACT

Understanding lava flow processes is important for interpreting existing lavas and for hazard assessments. Although substantial progress has been made for basaltic lavas our understanding of silicic lava flows has seen limited recent advance. In particular, the formation of lava flow breakouts, which represent a characteristic process in cooling-limited basaltic lavas, but has not been described in established models of rhyolite emplacement. Using data from the 2011–2012 rhyolite eruption of Puyehue-Cordón Caulle, Chile, we develop the first conceptual framework to classify breakout types in silicic lavas, and to describe the processes involved in their progressive growth, inflation, and morphological change. By integrating multiscale satellite, field, and textural data from Cordón Caulle, we interpret breakout formation to be driven by a combination of pressure increase (from local vesiculation in the lava flow core, as well as from continued supply via extended thermally preferential pathways) and a weakening of the surface crust through lateral spreading and fracturing. Small breakouts, potentially resulting more from local vesiculation than from continued magma supply, show a domed morphology, developing into petaloid as inflation increasingly fractures the surface crust. Continued growth and fracturing results in a rubbly morphology, with the most inflated breakouts developing into a cleft-split morphology, reminiscent of tumulus inflation structures seen in basalts. These distinct morphological classes result from the evolving relative contributions of continued breakout advance and inflation. The extended nature of some breakouts highlights the role of lava supply under a stationary crust, a process ubiquitous in inflating basalt lava flows that reflects the presence of thermally preferential pathways. Textural analyses of the Cordón Caulle breakouts also emphasize the importance of late-stage volatile exsolution and vesiculation within the lava flow. Although breakouts occur across the compositional spectrum of lava flows, the greater magma viscosity is likely to make late-stage vesiculation much more important for breakout development in silicic lavas than in basalts. Such late-stage vesiculation has direct implications for hazards previously recognized from silicic lava flows, enhancing the likelihood of flow front collapse, and explosive decompression of the lava core.

INTRODUCTION

Studies of hazards from silicic volcanic eruptions usually focus on explosive activity partly because effusive silicic eruptions are rare events. However, the emplacement of rhyolite lava flows has been previously associated with hazards such as explosions from their surface (Jensen, 1993; Castro et al., 2002), lava flow front collapse (Fink and Manley, 1987; Baum et al., 1989), and the potential generation of pyroclastic density currents (Fink and Kieffer, 1993). Of six such effusive eruptions in the 20th and 21st century (Katsui and Katz, 1967; Reynolds et al., 1980; Fierstein and Hildreth, 1992; Singer et al., 2008; Bernstein et al., 2013; Tuffen et al., 2013), three occurred at Puyehue-Cordón Caulle, southern Chile (in 1921–1922, 1960, and 2011–2012; Katsui and Katz, 1967; Lara et al., 2004; Singer et al., 2008; Tuffen et al., 2013). Thus, for contemporary hazard assessment, as well as for interpreting prehistoric deposits, improving our understanding of silicic lava emplacement processes may be more pressing than previously considered.

Lava flows initially advance in the direction of steepest gradient and their preliminary paths are thus relatively easy to forecast. However, after the lava flow front advance ceases, secondary lava flows, or breakouts, can form if effusion continues. Throughout this study we consider a breakout to be a new, morphologically distinct region of lava flow advance, formed from the core of an otherwise stopped or slowed portion of the lava flow. Such breakouts extend or widen the inundated area and uncertainties in where they will occur pose a challenge for forecasting lava inundation hazard. In basaltic lava flows, continued supply of mobile lava to a stalled flow front leads to inflation, and breakouts occur through rupturing of the surface crust (e.g., Walker, 1971; Kilburn and Lopes, 1988; Blake and Bruno, 2000; Applegarth et al., 2010b). Flow lengthening can be substantial when such breakouts are long-lived and fed by thermally preferential pathways that mature into lava tubes (e.g., Calvari and Pinkerton, 1998). However, breakouts in silicic lava flows have only been identified from a collapsed portion of a dacite lava flow margin on Santiaguito volcano, Guatemala (Harris and Flynn, 2002; Harris et al., 2004). Consequently, little is known about breakouts in silicic lavas. Here, we present the first conceptual model for their formation and consider the processes involved.

Previous studies of silicic lavas have interpreted their emplacement in terms of the slow spreading of crystal-poor domes, e.g., for Holocene rhyolite lava flows in the western USA (Fink, 1980a, 1980b, 1993; DeGroat-Nelson et al., 2001) and older rhyolites in Australia (Dadd, 1992; Smith and Houston, 1995) and

†n.magnall@lancaster.ac.uk

GSA Bulletin; January/February 2019; v. 131; no. 1/2; p. 137–154; https://doi.org/10.1130/B31931.1; 13 figures; 2 tables; Data Repository item 2018238; published online 15 August 2018.

New Zealand (Dadd, 1992; Stevenson et al., 1994a, 1994b). As a lava flow advances, cooled surface fragments cascade down the lava flow front and are overridden by the core in a tank-tread-style motion typical of block and 'a'ā lava flows (Fink, 1983; Harris et al., 2004). Rhyolite flows form a cooled surface crust that buckles into ogives as the lava flow front slows (Fink, 1980a; Castro and Cashman, 1999). The crust insulates the lava flow core, potentially maintaining core mobility long after effusion ceases (Manley, 1992; Farquharson et al., 2015). Just as for basalts, the crust can therefore exert a controlling influence on lava flow advance and emplacement (Magnall et al., 2017), making the formation of breakouts a possibility. Although a lobate lava flow front (Bonnichsen and Kauffman, 1987; Manley, 1996) and late-stage features such as pumice diapirs (Fink, 1980b; Fink and Manley, 1987) have been previously observed in rhyolite lava flows, breakout processes have not been discussed for rhyolite lava flows. Nevertheless, aspects of these processes could be linked; pumice diapirs are inferred to be caused by vesiculation of the flow core and buoyant rise to the surface, and vesiculation may also be important in breakout formation.

Advances in our understanding of the emplacement of silicic lava flows have been hampered by their infrequency. The 2011–2012 rhyolite eruption of Puyehue-Cordón Caulle in Chile (69.8–70.1 wt% SiO_2; Castro et al., 2013) enabled some of the first detailed scientific observations of emplacement processes. This lava flow produced numerous breakouts and provides a new resource to assess breakout processes in a cooling-limited rhyolite lava flow. Here, we use satellite and field observations to understand the processes occurring prior to, and during, breakout formation. Microtextural characteristics from thin sections and synchrotron computed tomography help constrain crystallization and vesiculation histories, allowing us to create a conceptual model for breakout formation in a silicic lava flow.

THE 2011–2012 ERUPTION OF PUYEHUE-CORDÓN CAULLE

Puyehue-Cordón Caulle is a basaltic to rhyolite volcanic complex located in the southern volcanic zone of the Chilean Andes (Fig. 1). The 2011–2012 eruption began on 4 June 2011, producing a 15-km-high Plinian ash col-

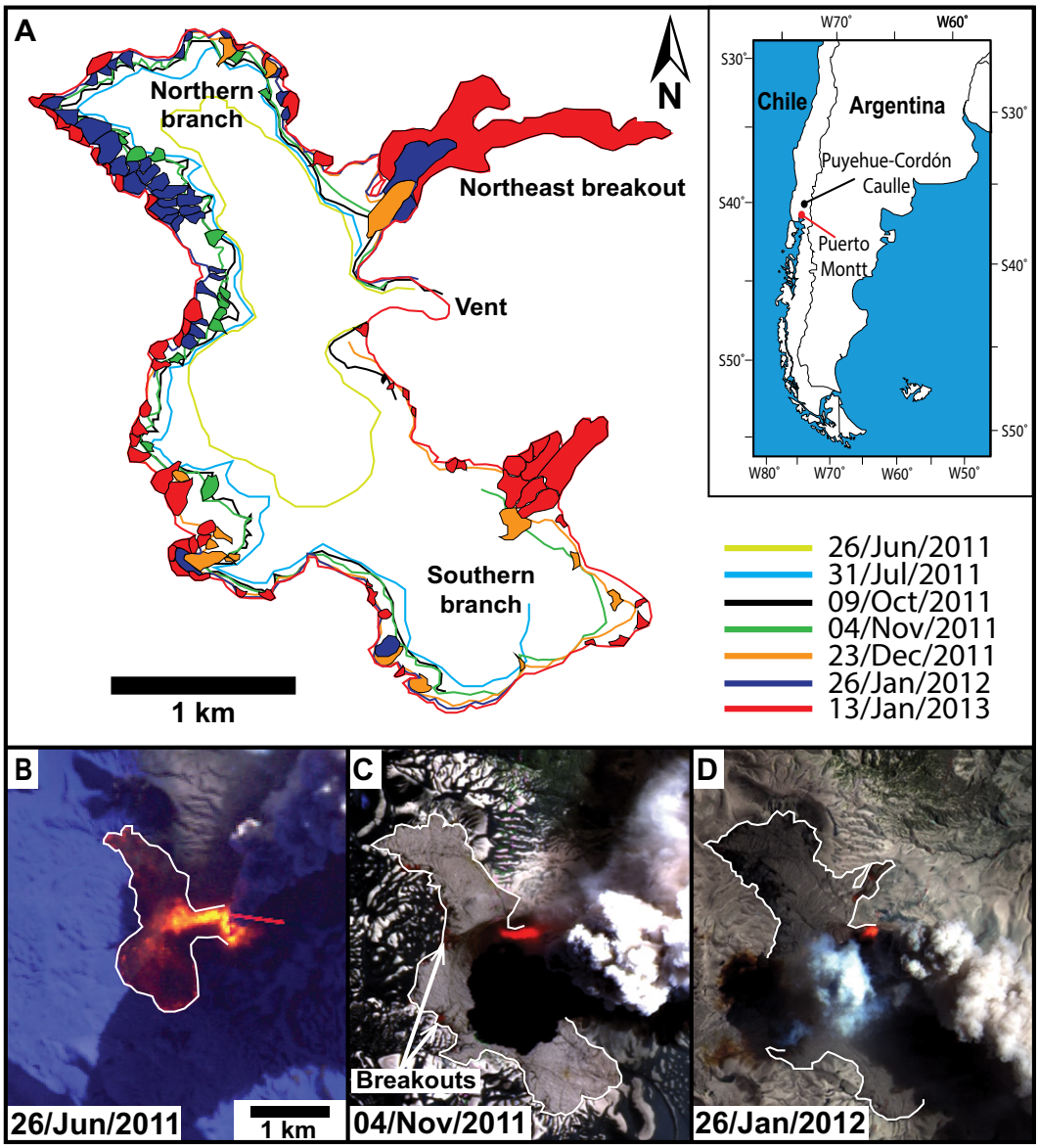

Figure 1. Lava flow outlines of the 2011–2012 Cordón Caulle lava flow, southern Chile derived from Landsat 5 and Earth Observing (EO-1) Advanced Land Imager (ALI) satellite images (NASA, 2011c, 2011b, 2011a, 2011e, 2011d, 2012, 2013), data available from the U.S. Geological Survey. (A) Position of the lava flow front through time and the timing of breakout formation. (B) Landsat 5 image of the initial lava effusion. The red line trending E-W is likely a saturation effect/anomaly. (C) EO-1 ALI image of the initial breakout formation. (D) EO-1 ALI image showing continued breakout formation. A number of separated lava flow outlines can be found in Data Repository file 1 (see footnote 1).

umn (Castro et al., 2013), followed by coupled effusive-explosive activity with simultaneous emission of lava and pyroclasts from a common vent (Castro et al., 2013; Schipper et al., 2013; Tuffen et al., 2013; Bertin et al., 2015). Initial discharge rates were up to 50–70 m^3 s^{-1} but reduced to ~10–20 m^3 s^{-1} after ~30 days (Bertin et al., 2015; Coppola et al., 2017). Lava effusion was identified first in synthetic aperture radar satellite images on 19 June 2011 (Bignami et al., 2014) and formed two branches that advanced to the north and south, before stalling and forming numerous (>80) breakouts from the lava flow front and margins (Tuffen et al., 2013; Magnall et al., 2017). Although the eruption ended between 15 March 2012 and 24 April 2012, as indicated by the cessation of seismicity at the vent (SERNAGEOMIN/OVDAS, 2012; Tuffen et al., 2013) and the end of ash generation (Global Volcanism Program, 2012), respectively, some local areas of advance were still observable in January 2013 (Tuffen et al., 2013).

METHODOLOGY

Our multiscale data analysis of breakouts and the main lava flow brings together satellite imagery, digital elevation models (DEMs), 3-D photogrammetry models, as well as scanning electron microscopy (SEM) and synchrotron X-ray computed tomography (CT) imaging of samples collected in the field. Fieldwork at Cordón Caulle was carried out during and after the eruption, in 2012, 2013, and 2015 (always in January), and allowed for sample collection and a detailed examination of the structure of the lava flow and breakout morphology. Approximately 50 in situ samples were collected from the lava flow front and top surface, and from fallen fragments at the lava flow front. Fieldwork in 2015 was complemented by aerial photographs acquired from a helicopter.

Satellite Imagery

The lava flow evolution was tracked using satellite images from the Earth Observing 1 (EO-1) Advanced Land Imager (ALI; e.g., Digenis et al., 1998), Landsat 5 and 7 Enhanced Thematic Mapper Plus (ETM+), and the Terra Advanced Spaceborne Thermal Emission and Reflection Radiometer (ASTER; Yamaguchi et al., 1998). EO-1 and Landsat data are available from the U.S. Geological Survey, and ASTER data are distributed by the Land Processes Distributed Active Archive Center (LP DAAC), located at the U.S. Geological Survey Earth Resources Observation and Science Center (USGS/EROS), Sioux Falls, South Dakota, USA, (http://lpdaac.usgs.gov). Google Earth imagery was also used. All images, except those from Google Earth, were processed in ENVI to create true color images, or false color images from the visible, near infrared (VNIR) and the shortwave infrared (SWIR) bands, with spatial resolutions between 15 and 30 m. Where possible, the resolution was improved by combining the images with their corresponding panchromatic image (EO-1 10 m resolution, Landsat 7 ETM+ 15 m resolution) using the NNDiffuse-PanSharpening function in ENVI, allowing the detection of lava flow features larger than a few tens of meters across. The resulting imagery was imported into ArcGIS and the coregistration refined using fixed points, such as roads, lakes, and older lavas that were assumed to be stationary throughout the duration of the eruption.

The qualitative thermal evolution of the lava flow surface was tracked using thermal infrared (TIR) images from Landsat 5, 7 (Band 6), and ASTER (L1T) sensors, visualized in ArcGIS. These TIR images have coarser resolution (Landsat 30 m, ASTER 90 m) than their VNIR and SWIR counterparts, and dense time-series analyses were restricted by the eruptive plume and cloud cover, which often obscured parts of the lava flow.

3-D Models from Field Photos and DEMs

To determine the detailed structure of five selected breakouts, 3-D surface models were generated from ground-based field photos using structure-from-motion photogrammetry (e.g., James and Robson, 2012). Approximately 100 photos were taken on foot at regular intervals in an arc around a feature of interest using a Canon 450D digital single-lens reflex camera, with a fixed focus 28 mm lens. The photos were processed in Agisoft PhotoScan Professional (v1.3.2) to generate dense 3-D point clouds, which were manually cleaned to remove outlying points. The models were scaled by recognizing common features in georeferenced satellite images of the lava, giving an overall scale accuracy of 5–10%, suitable for qualitative assessments of lava morphology. Cross sections were obtained by first gridding the 3-D point clouds into 10-cm-resolution DEMs, then extracting the sections.

The morphology of the largest breakouts could not be observed fully from the ground so such areas were analyzed using a post-eruption Pléiades DEM (Elevation 1 data set) with a 1 m horizontal resolution and 1.5 m horizontal and vertical accuracy. The DEM was generated from stereo satellite images, so the bases of deep and narrow features, such as fractures, may not have been reconstructed due to being occluded in either one or both images. 2-D profiles were extracted by sampling the DEM at a 2 m resolution, to help reduce the noise from the highly uneven and blocky nature of the lava surface.

Samples and Thin Sections

Microstructural characterization of key representative lava facies was carried out by SEM analysis using a LEO 435VP variable pressure digital scanning electron microscope. Mineral identification was aided by qualitative observation of energy-dispersive X-ray spectra recorded simultaneously during SEM observation, using an Oxford Instruments INCA energy-dispersive X-ray microanalysis (EDXA) system. Images were captured from thin sections in backscattered electron mode for further image analysis, which included determining microlite contents using CSDCorrections software (Higgins, 2000). Up to ~400 microlites in SEM images of ~15 representative samples (from four breakouts) were first isolated by tracing the crystal edges. The resulting image was analyzed in ImageJ and CSDCorrections to determine total microlite volume fractions. The crystal volume fractions presented here (as percentages) are the stereologically corrected intersection data from CSDCorrections (Higgins, 2002) and have been compared with similar data from Schipper et al. (2015). Vesicularity (Table 1) was estimated from the 2-D vesicle fraction in SEM images using ImageJ. This straightforward method only gives an approximate value of vesicularity, but enables comparisons among different lava facies.

Textures in breakout samples were examined in 3-D using synchrotron X-ray source

TABLE 1. LAVA FLOW FACIES MICROLITE CONTENT AND VESICULARITY

Facies	Microlite content (%)	Bulk crystallinity, X-ray diffraction (%)*	Vesicle sizes (mm)	Vesicularity (%)
Pyroclastics	N/A	~10–30	N/A	N/A
Surface pumice	<5	N/A	Up to 5 long, 0.2 wide.	~30 (1–2 m depth)
Vent lava	20–25	~20–25	0.1–5 diameter.	~30–50 (surface)
Breakout lava	30–40	~50	Elongate: 0.2–10 long, 0.03–0.58 wide. Undeformed: 0.7–7 diameter.	~15–30 (highest with undeformed vesicles)
Main channel core	70–80	~70–100	<0.05 diameter (sparse up to ~1 diameter)	~5

*Schipper et al. (2015).

computed tomography (CT), performed at the Australian Synchrotron (Clayton, Victoria) in hutch 3B of the Imaging and Medical Beamline. Images were captured using the in-house "Ruby" detector, with X-ray energy of 45 keV. Scans included the collection of 1800 radiographs with 0.3 s exposure time over 180° rotation and a pixel size of 13.7 µm. The length of the samples required three partially overlapping scans, which were reconstructed separately using the in-house MASSIVE supercomputing cluster, and then stitched together using ImageJ (Schneider et al., 2012). All renderings were performed with the Drishti visualization software package (Limaye, 2012).

RESULTS

Lava Flow Emplacement

Satellite observations from EO-1 ALI have been previously used to show that the ~40-m-thick lava flow was emplaced into a topographic depression and, within ~600 m of the vent, split into two main branches 600–1000 m wide, of which one advanced north and the other south (Fig. 1; Magnall et al., 2017). The southern branch moved down a relatively constant slope of ~7° before interacting with a topographic barrier toward the end of its emplacement. The northern branch was similarly impeded by a ridge within the first 30–60 days of the eruption (from the eruption start on 4 June 2011; Magnall et al., 2017). This ridge halted the northern advance of the lava and led to a widening of the lava flow front (~200 m, yellow and turquoise outlines in Fig. 1A).

The first breakouts were observed at the western margin of the northern branch, 153 days after the eruption started (90–120 days after stopping against a ridge; Fig. 1C), and following the development of flow front lobes 50–250 m wide and 50–200 m long separated by large fractures that extended 25–200 m backward from the flow front (Fig. 1C, Data Repository file 1[1]). Here, a lobe is distinguished from a breakout through forming via continued but spatially uneven advance of a lava flow front, rather than the effusion of core material from a slowing or stalled lava flow margin. In optical satellite images (Figs. 1C, 1D), the breakouts appear darker than the main lava flow but, in ASTER TIR data, breakouts appear as bright features at the lava flow front (Figs. 2C, 2D; Coppola et al., 2017). Some of the earliest breakouts were subsequently enveloped by the forward advance of the main branches (Fig. 1), and became subsumed into the main body of the lava flow. Most breakouts range in size from ~15 to 40 m thick, 30 to 150 m wide, and 30 to 450 m long; the longest occur in areas with little topographic constraint. Breakouts from the southern branch developed predominantly from its sides, following lobe generation as seen in the northern branch; some small breakouts (up to 60 m long and 50 m wide) formed from the front toward the end of the eruption (Fig. 1A).

After 200 days (first observed 23 December 2011, 110–170 days after stopping against a ridge), a breakout formed from the eastern margin of the northern branch, and developed a substantial length (~2 km; Magnall et al., 2017); hereafter this breakout is referred to as the northeast breakout (Fig. 1A). This new breakout entered a relatively steep (~15°) and narrow (200–350-m-wide) valley, and halted only when the eruption ended (Fig. 1). In TIR imagery, the northeast breakout is brighter than the bulk of the main lava flow throughout its lifetime and for several months after the eruption ceased (Figs. 2B, 2C). The breakout developed distinct levees and appears to have sections of partially drained channel, which likely relates to this breakout being volume limited and stopping once supply to it ended. After the establishment of this breakout, there was a noticeable reduction in the rate of initiation of new breakouts from the northern branch (Fig. 1). Between December 2011 and January 2012, tens of breakouts formed from the northern branch but, after 26 January 2012, when the northeast breakout had become established (Fig. 1), only five new breakouts were formed in the following two months before effusion ended on 15 March 2012.

Breakouts continued to form and evolve for some time after the eruption ended. In the western margin of the northern branch, some of the breakouts continued to grow (Figs. 3B, 3C), but some showed only limited post-eruption advance (<50 m). Instead, fractures (up to ~100 m long) developed within the breakouts and parallel to their advance direction (Figs. 3B, 3C). From the southern branch, ~5 new breakouts formed at its eastern margin (Figs. 1A and 3) and developed similar, long fractures (up to 300 m long; Fig. 3E). One of these breakouts was observed advancing in January 2013, ten months after the eruption ended (Tuffen et al., 2013; Farquharson et al., 2015).

In total, ~90 breakouts formed (Fig. 1), accounting for ~12% (±2%) of the total lava flow volume (as estimated from the areal coverage in satellite imagery and assuming an average breakout thickness of ~80% of the main branch thickness, i.e., ~32 m). The volume of the breakouts is thus equivalent to a 4 m increase in thickness of the main branches.

Lava of the Main Northern and Southern Branches

The main northern and southern branches have coarse, red-brown rubble surfaces composed of fragments up to several meters across, and are bounded by steep and blocky levees, comprising a mixture of loose rubble and coherent, dense, core lava (Fig. 4). Parts of the lava surface near the vent appear lighter in color and less blocky and represent areas where collapsed portions of the tephra cone have been rafted on the lava surface. The surface of the lava is systematically folded into ogives with a wavelength of ~40 m and an amplitude of order several meters (Magnall et al., 2017). The lava flow surface is also split by fractures, most of which are oriented perpendicular to the lava flow front (Data Repository file 1; see footnote 1), tens to hundreds of meters long and several meters deep, and many expose a surface crust of coherent and dense lava beneath the loose surface fragments.

Textures of the Main Branch Lava

The fragments that comprise the top surface and lava flow front of the main branches are a mixture of dark vesicular and glassy rhyolite, golden colored lava-flow-top-pumice, and gray to red-brown dense core lava (Fig. 4). The dark glassy rhyolite is the most abundant on the lava surface, whereas the lava-flow-top-pumice occurs as isolated patches (~1–20 m wide) on the lava surface (Figs. 4B, 4E, and 4F). The core of the lava is exposed in areas where portions of the lava flow front and margins have collapsed (Fig. 4A) and is microcrystalline, with sparse sub-millimeter vesicles (Table 1; Figs. 4C, 4D). Millimeter-spaced, parallel, platy fractures, associated with vapor-phase cristobalite formation (Figs. 5A, 5B; Schipper et al., 2015), are laterally extensive over tens of centimeters (Fig. 4D).

Microstructure

Samples from the northern and southern branches include those from the lava flow core, surface, and lava at the vent. SEM analysis identified two main crystal populations in this lava, phenocrysts and microlites. The core samples are microcrystalline (~70–80 vol%) and display the extensive millimeter-spaced platy fractures. In some cases, the fractures have a number of

[1]GSA Data Repository item 2018238, (1) Separated flow outlines showing ogive and fracture networks on the surface of the Cordón Caulle lava flow; (2) 3-D PDF of the 3-D model in Figure 7 (note this only works in AdobeAcrobat); (3) Timeline of feature development, and crystallization history, of the Cordón Caulle rhyolite lava flow, is available at http://www.geosociety.org/datarepository/2018 or by request to editing@geosociety.org.

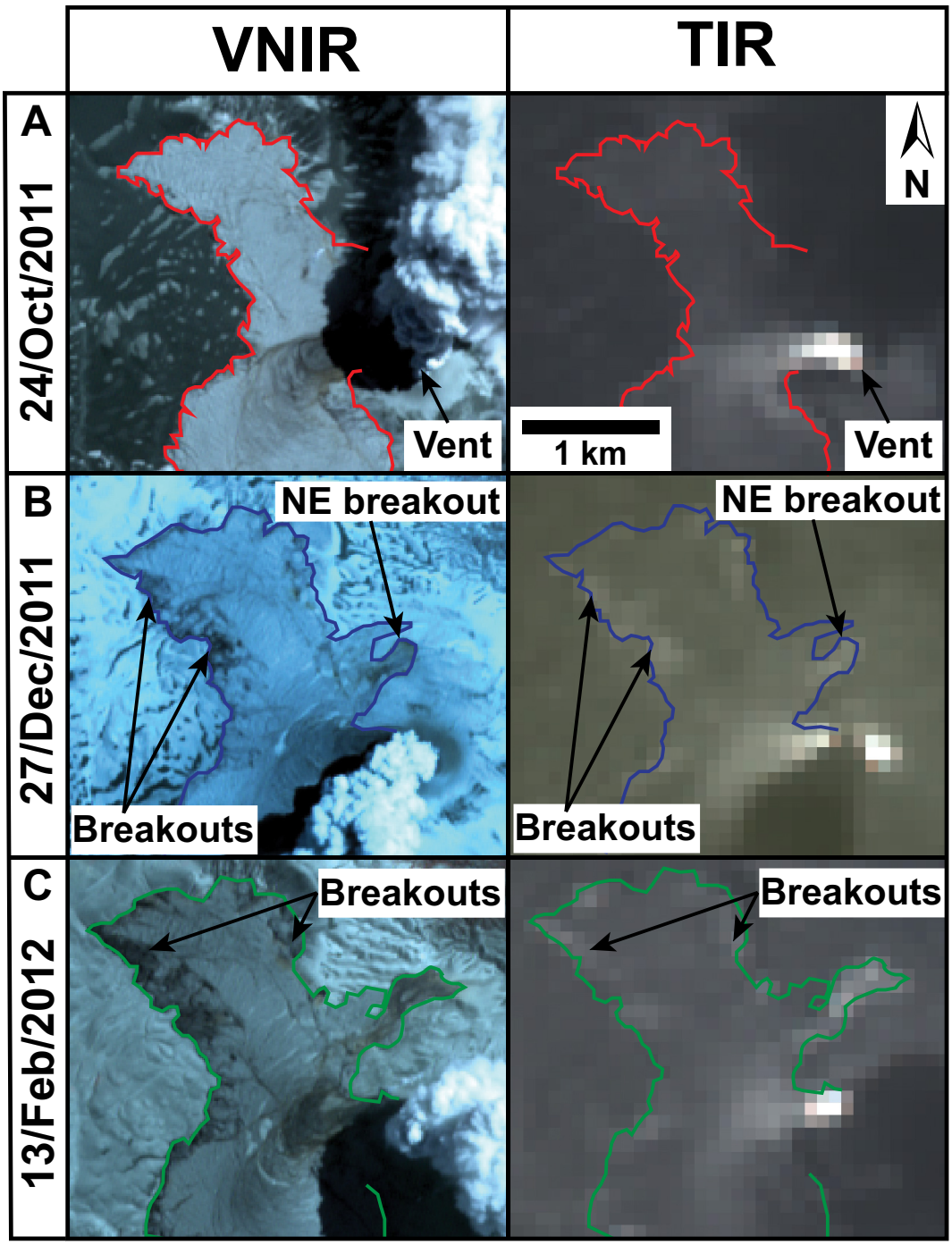

Figure 2. Advanced Spaceborne Thermal Emission and Reflection Radiometer (ASTER) visible, near infrared (VNIR) and corresponding thermal infrared (TIR) images of the 2011–2012 Cordón Caulle lava flow, southern Chile (NASA/METI, 2011a, 2011b, 2012). These data are distributed by the Land Processes Distributed Active Archive Center (LP DAAC), located at the U.S. Geological Survey Earth Resources Observation and Science Center (USGS/EROS), Sioux Falls, South Dakota, USA, (http://lpdaac.usgs.gov). (A) Early phases of the lava emplacement prior to breakout formation. (B and C). Later phases of lava emplacement when breakouts were observed. Breakouts correspond to bright spots at the lava flow front in the TIR images. The northeast breakout is visible in images B and C. The pixelation of the TIR images relates to the 90 m pixel size of the ASTER TIR data.

s-shaped shear arrays (0.5–1 mm long and 0.05–0.1 mm wide, Fig. 5A) and, in many places, the two sides of the fractures are connected by thin (1–8-µm-wide) glassy filaments.

The surface samples from the main branches comprise vesicular flow-top-pumice (Figs. 5C, 4B, and 4F). Pumice samples have highly contorted, elongate vesicles (Table 1; Fig. 5C) and a microlite volume of ~5 vol%. Samples from the vent represent some of the last effused lava. The samples are vesicular (Table 1) and have poorly developed flow-bands marked by subtle variations in microlite content (~5 vol% variation, Fig. 5D). The microlite content of the vent samples is ~20–25 vol% (Table 1).

Breakouts

The large number of breakouts gives the overall lava flow a lobate outline in plan view, and their darker, more slabby and blocky morphology contrasts with the redder, more rubbly surface of the main branches (Tuffen et al., 2013). Analysis of breakouts used a mixture of satellite imagery (>50 breakouts analyzed), aerial photography (10 breakouts), topographic cross sections from a high-resolution DEM (20 breakouts), detailed field observations (20 breakouts), and 3-D photogrammetry models (5 breakouts). Although a comparison of bulk composition between breakouts and main branch samples has not been conducted, analyses of groundmass glass of breakout and main branch lava shows

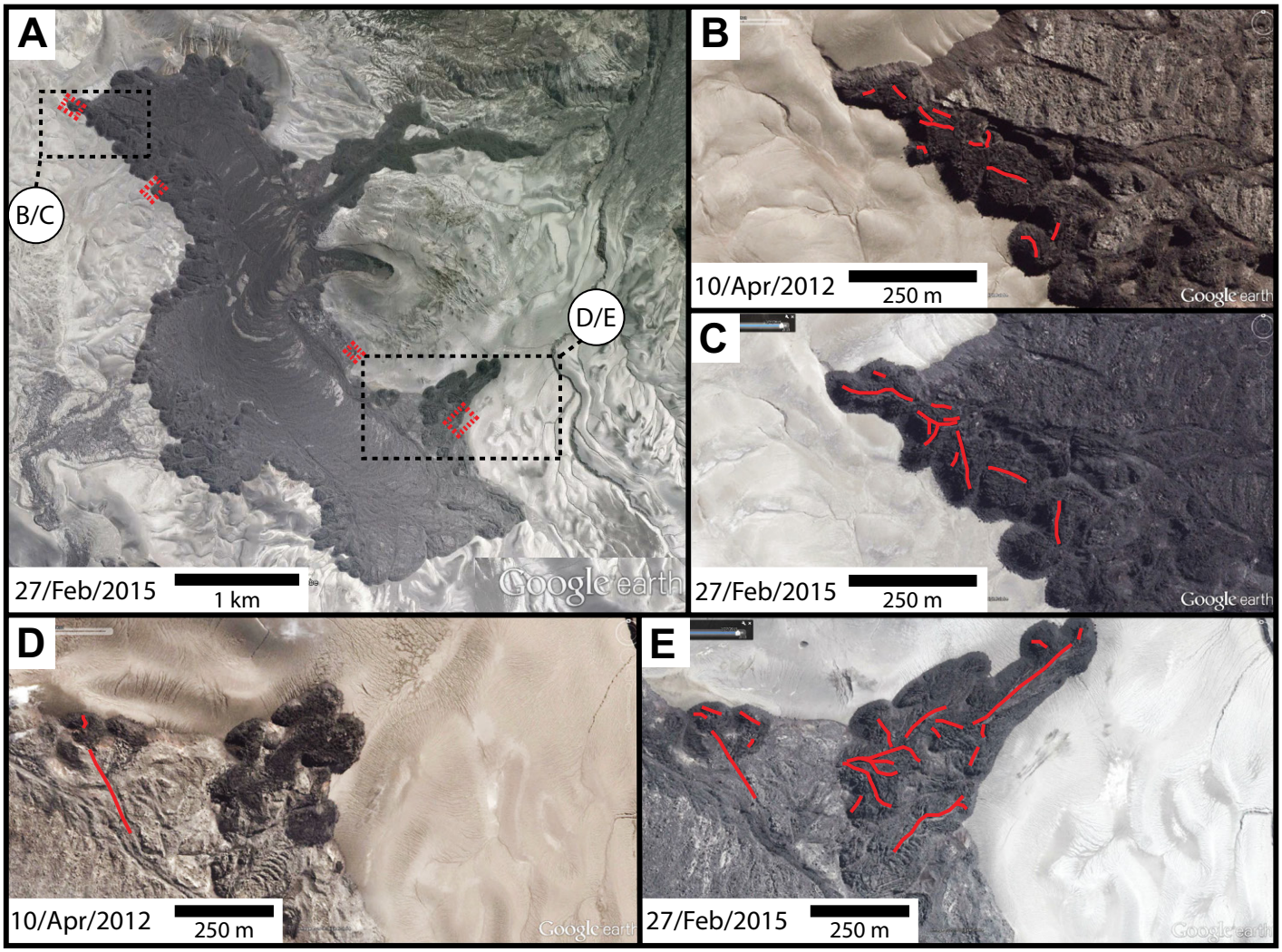

Figure 3. Google Earth images of the 2011–2012 Cordón Caulle rhyolite lava flow, southern Chile (DigitalGlobe, 2012, 2015). (A) The two boxes labeled B/C and D/E show the location of images B, C and D, E, respectively. The red boxes show the locations of the breakouts in Figure 8. (A, C, and E) Images are from 2015, several years after the eruption ended. (B and D) Images are from 2012, one month after the eruption ended when the lava flow was still advancing locally. After the eruption ended, breakouts continued to form from the lava flow front and margin. Red lines show the locations of fractures, some of which continued to form after the eruption ended as the breakouts evolved.

little variation (Schipper et al., 2015). Phenocryst assemblages (constituting plagioclase, pyroxene, magnetite, and ilmenite) were also found to be identical in lava samples and pyroclasts from the eruption (Castro et al., 2013).

Sources

Field and satellite observations suggest that breakouts were sourced from either (1) the base or part way up the lava flow margin, or (2) large fractures extending back into the main branches. For some breakouts (particularly those in the southern branch that was obscured by the eruptive plume in satellite images), the source region is difficult to determine. Some source regions were also sites of preferential outgassing, indicated by a white precipitate covering many of the nearby fragments (Fig. 6A) and associated gas plumes observed in 2012. Similar outgassing was observed at stalled portions of the main branches (Fig. 6C).

Small breakouts from the base of the lava flow margin (Fig. 6A) emerged as thin (~10–15-m-thick) lava bodies that then underwent inflation and advance. In some cases, a region of the main branch behind these breakouts subsided to form an amphitheater-like structure up to 10 m deep (Figs. 6A and 7). Such amphitheaters are typically associated with the smallest breakouts, suggesting that the breakout is sourced by drainage from only a limited area of the main branch rather than being connected to an extended, and more continuously supplied, source (Fig. 7).

Other breakouts were sourced from fractures (≤4 m deep, 5–10 m wide) that extended ~50–150 m back into the main branch (Fig. 6B). The satellite data showed that breakouts from fracture zones were preceded by the formation of lobes and extensional fractures at the lava flow margin (Fig. 1, Data Repository material [see footnote 1]). Breakouts sourced from these fractured regions formed the largest breakout complexes (multiple potentially branched breakouts, up to hundreds of meters long).

Morphologies

The breakouts show a range of morphologies, which we describe in four general classes: domed, petaloid, rubbly, and cleft-split (Table 2; Fig. 8).

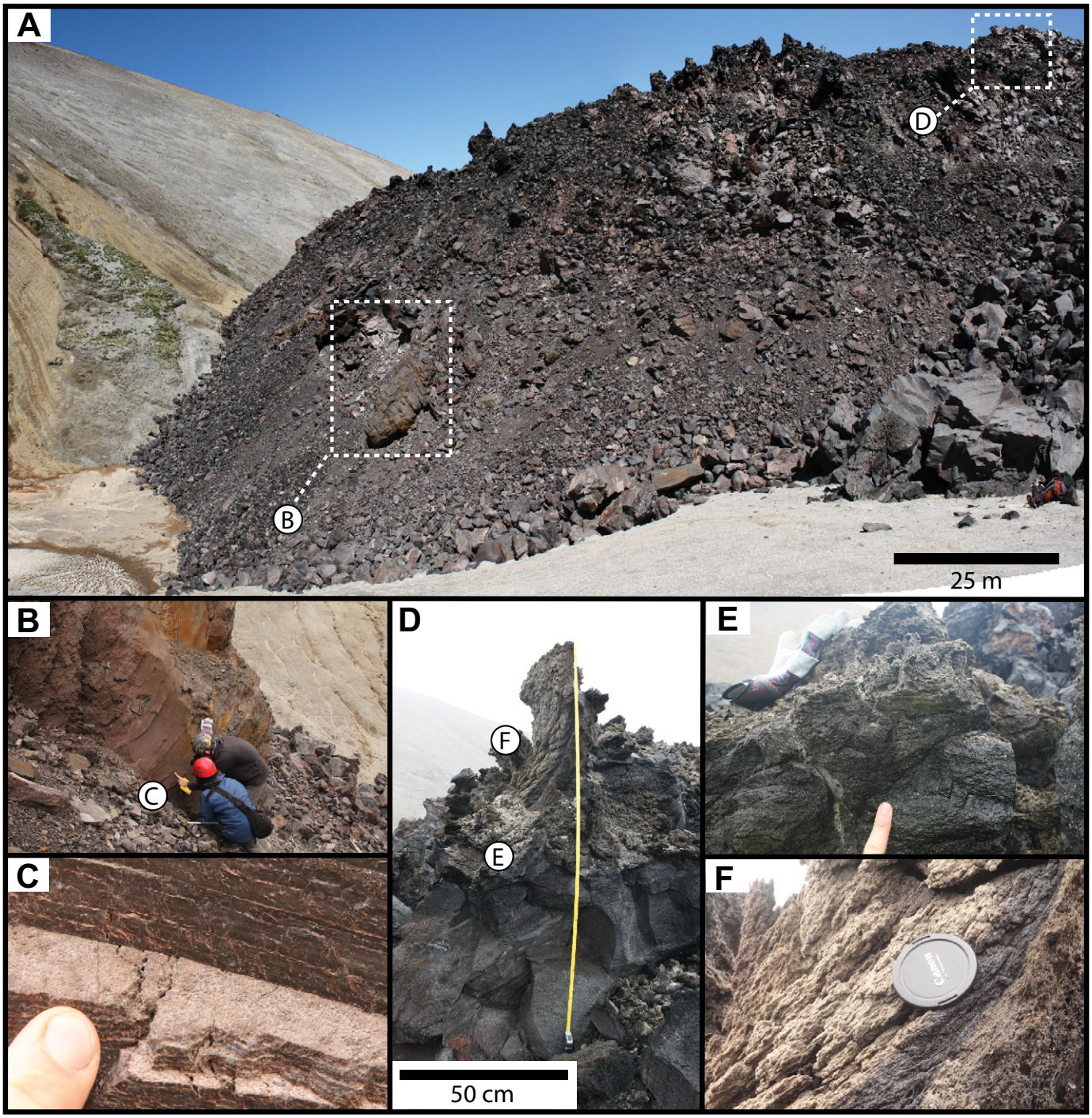

Figure 4. (A) Part of the lava flow front of the northern branch of the 2011–2012 Cordón Caulle lava flow, southern Chile. (B and C) The crystalline core of the lava flow is visible where large sections of the lava flow front collapsed. The core is dense with very few vesicles and has closely spaced platy fractures that are filled with cristobalite. (D, E, and F) In the surface crust of the main branch, the denser crust grades into the much more vesicular flow-top-pumice.

Domed breakouts are usually sourced from the base or part way up the lava flow margin (Figs. 7 and 8). These breakouts have a domed shape and are wider than they are thick (Fig. 8). The surface comprises slabs (several meters across, Table 1) of dark, glassy, surface crust (Figs. 7 and 8), which retain a jigsaw-fit pattern but are disrupted by fractures tens of meters long and several meters deep. Commonly, sections of the breakout have collapsed, to expose the lighter gray-colored core lava.

Petaloid breakouts are steep sided and have an uneven surface due to a large number of upturned surface slabs (Fig. 8), which are up to tens of meters tall (Table 2) and can form prominent spines. Such spines have a dark, typically polygonally jointed, glassy surface that grades

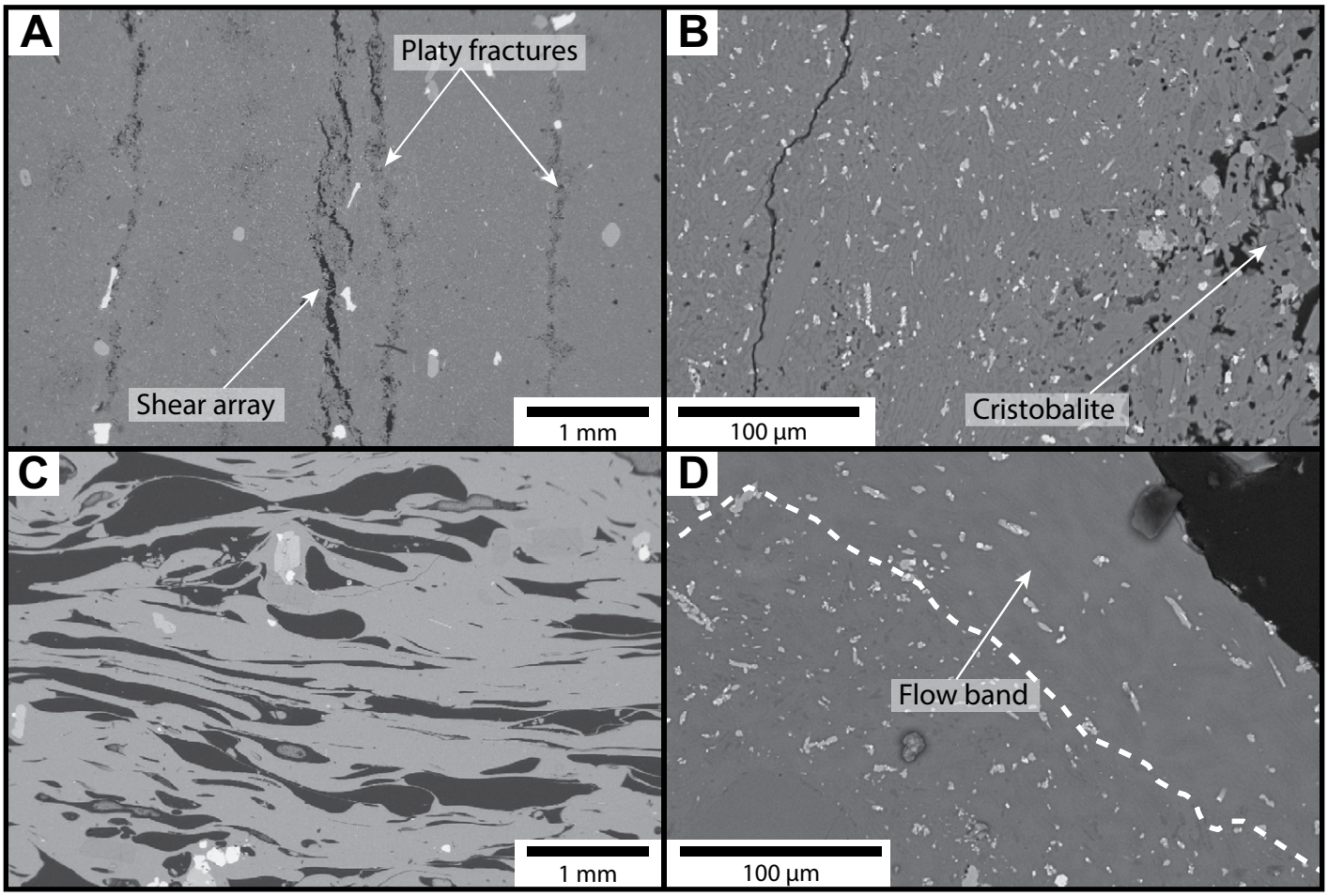

Figure 5. Scanning electron microscopy images of main branch samples from the 2011–2012 Cordón Caulle lava flow, southern Chile. (A) Crystalline core of the lava flow; platy fractures that are infilled with cristobalite and are variably healed. Some shear zones are also found within these fractures. (B) Crystalline lava flow core; cristobalite infills void spaces and platy fractures. The cristobalite is difficult to see and is distinguished through qualitative analysis of X-ray spectra. (C) Glassy flow-top-pumice (from Fig. 8E) with a large number of elongate and collapsed vesicles. (D) Flow-band marked by a variation in microlite content in a portion of the near-vent lava and separated by the dashed line.

into lighter colored core lava. Regions between the slabs and spines are filled with rubble (tens of centimeters to a meter across), and fragments form a relatively narrow (<10 m) talus apron surrounding breakouts. The surface slabs of petaloid breakouts are more isolated than in domed breakouts, but locally retain jigsaw-fit patterns.

Rubbly breakouts (including the large northeast breakout) have a surface that is almost entirely covered in rubble and disrupted slabs (Table 2; Fig. 8). The rubble comprises brecciated crust and core lava, and includes large slabs that are similar to the surface slabs and spines observed in petaloid breakouts (Fig. 8), giving an uneven surface profile. However, slabs are sufficiently disjointed that any semblance of a jigsaw-fit pattern is lost. Lateral collapses form larger talus aprons than around domed or petaloid breakouts (~20–40 m wide) and, in some cases, expose the lighter colored core lava (Fig. 8).

Cleft-split breakouts have a large central cleft that is orientated parallel to the direction of advance, typically tens of meters long and several meters deep, and runs most, or the entire length, of the breakout (Fig. 8). Cleft surfaces are striated on a decimeter scale, marking repeated transitions from rough to smooth fracture surfaces. Outside of clefts, the breakout surface comprises of either slabs or rubble (Table 2). Some of the most complex cleft-split breakouts are also branched and, in a few cases, subsidiary breakouts are observed (Fig. 8).

The four breakout morphologies present part of an evolutionary continuum and intermediate morphologies are also observed. For example, some rubbly breakouts show features associated with petaloid breakouts, such as disjointed slabs of surface crust amongst the rubble. Post-effusion satellite images of breakouts (Fig. 3) also demonstrate the continuing evolution of breakouts, whereby rubbly and petaloid breakouts develop into cleft-split morphologies (as indicated by the red lines in Fig. 3). Furthermore, the fracturing and upturning of surface slabs, associated with the transition from domed to petaloid morphologies, was observed during the eruption (Tuffen et al., 2013).

Textures of Breakout Lava

Breakouts comprise dark, glassy lava with a black scoriaceous surface crust that grades into a lighter gray interior (Figs. 9A, 9B). In hand-specimen, the lava is vesicular, with a mixture of undeformed, near-spherical and more elongate vesicles (Fig. 9C), with a greater number of undeformed vesicles near the surface. Beyond the

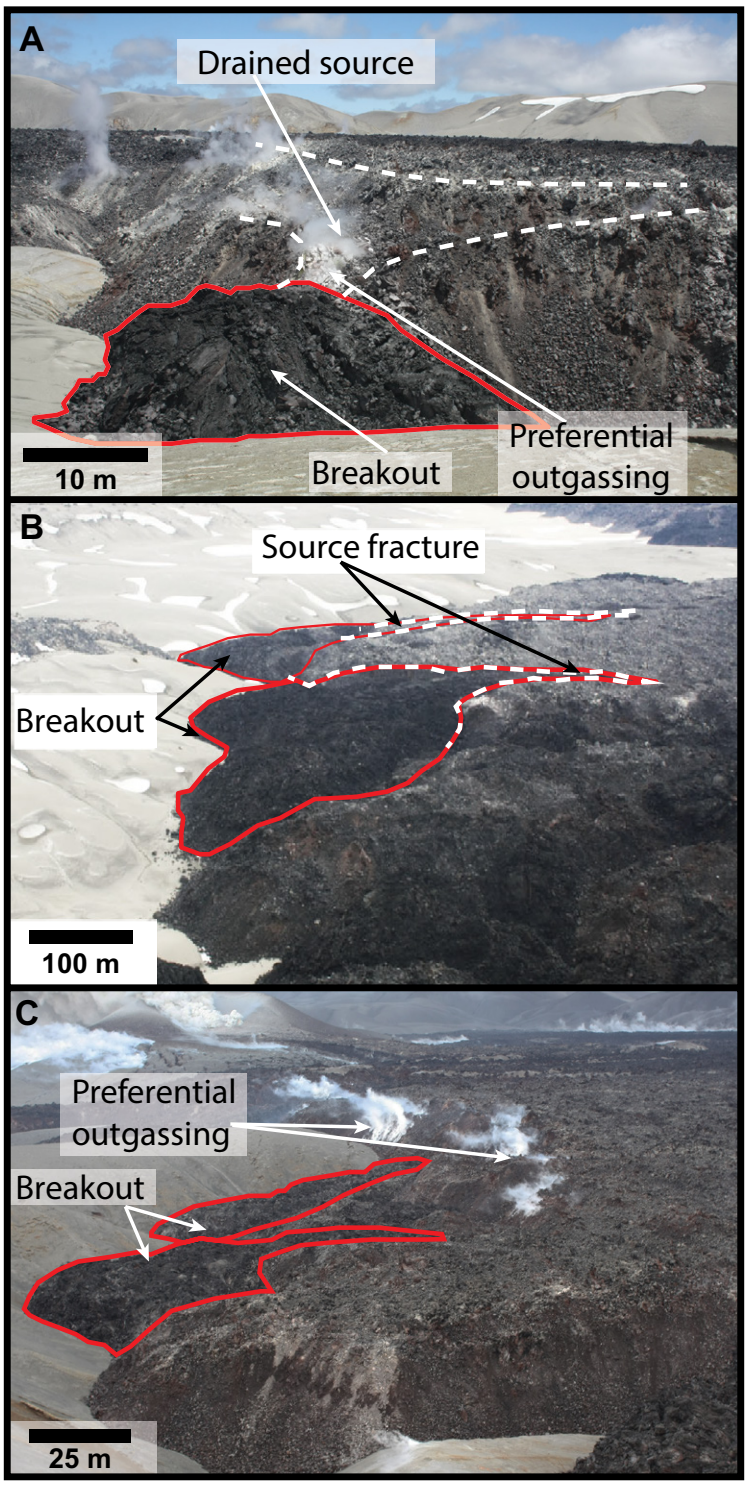

Figure 6. (A) Photo of a base-fed breakout at the margin of the southern branch of the 2011–2012 Cordón Caulle lava flow, southern Chile, in front of a drained amphitheater. The drained region is a site of preferential outgassing of the lava. (B) Aerial photograph of a breakout that originated from a large fracture in the surface of the lava flow. This fracture extended 50–150 m back into the main branches and the breakout emerged from this fracture. (C) Photo taken from a nearby highpoint of base-fed breakouts from the lava flow margin. Note the preferential outgassing at the lava flow front and behind the breakouts.

top few tens of centimeters of the surface crust, many of the vesicles display white walls, representing regions in which interstitial glass has been corroded during a vapor-phase cristobalite forming process (Schipper et al., 2015, 2017). Flow-bands are also common; lighter and darker bands are typically a few millimeters thick but laterally extensive over tens of centimeters (Figs. 9B and 9D). In many cases, these bands are folded and wrap around vesicles (Fig. 10D).

A slightly different texture is observed in one of the longest (400 m) rubbly breakouts at the western margin of northern branch. Here, the lava is glassy and has a large population of white-walled, corroded vesicles, typical of breakout lava, but is also cut by the millimeter-spaced platy fractures (coated and partially filled with cristobalite) that are most commonly associated with the core of the main branch (Fig. 9F). The texture represents an intermediate between that of the fractured main branch core and the vesicular breakout lava.

Microstructure

SEM images of breakout samples verify the presence of two vesicle populations and show the three crystal populations of phenocrysts, microlites, and devitrification-related crystalline masses. For the purposes of this study, the phenocrysts (<5 vol% of the lava) will not be assessed further as they are unlikely to have had much, if any, influence on emplacement processes. The microlites primarily comprise plagioclase, some of which are subtly zoned (Fig. 10E), and some pyroxenes as well as accessory apatite and metal oxides (Fig. 10E). Microlites are 2–10 µm wide and 5–50 µm long, and typically aligned parallel to the flow-bands. They comprise 30–40 vol% (measured from four breakouts with petaloid, rubbly, and cleft-split morphologies) in glassy flow-bands where devitrification crystallization is absent. The microlite abundance varies slightly (~5 vol%) between separate millimeter to submillimeter bands.

Darker, spherical, crystalline masses (0.03–0.4 mm diameter, Fig. 10), some of which surround vesicles (Fig. 10C), are found in the core of breakouts. These crystalline masses are surrounded by small vesicles or fracture networks 1–2 µm wide but lack the radiating crystal structure commonly observed in spherulites and are best classified as globulites, which form as a result of devitrification (Lofgren, 1971; Schipper et al., 2015). Globulites comprise ~70 vol% microlites (with overgrowths of 1–2 µm in width, Fig. 10F) and ~30 vol% cristobalite. Where globulites merge, they form substantial flow-bands up to several centimeters thick. Globulites are observed in all breakout samples except those from the quenched surface crust.

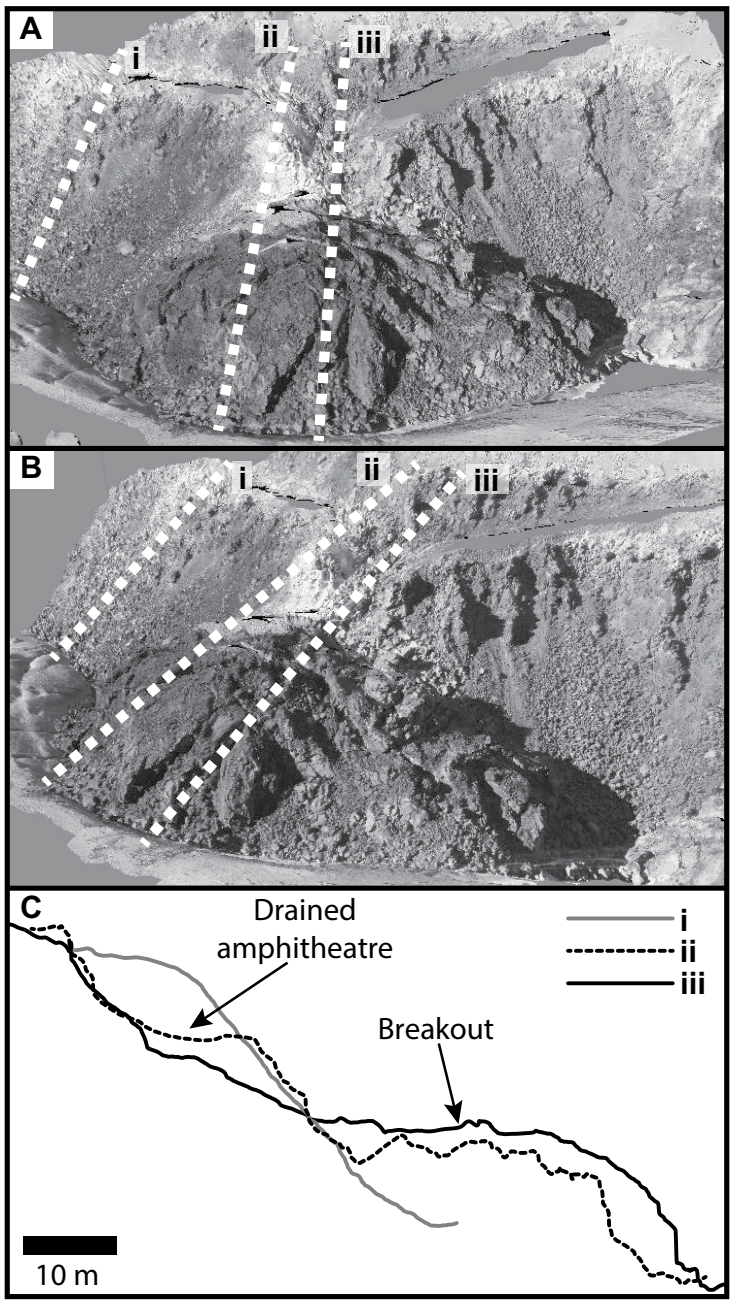

Figure 7. (A and B) 3-D structure-from-motion photogrammetry model of a domed breakout from the margin of the southern branch of the 2011–2012 Cordón Caulle lava flow, southern Chile. Lines i, ii, and iii show the approximate locations of the cross sections in C. The cross sections highlight a region of drained main branch behind the breakout. A section of main branch without a breakout is shown for comparison. A 3-D PDF of this photogrammetry model can be found in the supplementary material (Data Repository file 2; see footnote 1).

The two vesicle populations comprise (1) sheared, partially collapsed vesicles and (2) spherical and relatively undeformed vesicles, both of which can be observed in hand specimen (Fig. 9C), thin section (Figs. 10B–10D), and CT renderings (Fig. 11). Sheared vesicles are elongate (Table 1) and many are pinched at one end, suggesting partial collapse. Some form vesicle trails (Fig. 10B), but many are found in isolation (Fig. 10C). Sheared and collapsed vesicles are more abundant in samples from deeper in breakouts than at the surface. In contrast, spherical (Table 1) and undeformed vesicles (Figs. 9C, 10D, and 11) are found throughout most breakouts but are more common near the surface and in flow-bands (Fig. 11A).

Many of the vesicles located deeper within the breakouts have uneven walls (Fig. 11C) that have undergone partial preferential dissolution of interstitial groundmass glass due to gas flux through the vesicle network (Schipper et al., 2015). Dissolution led to the formation of a diktytaxitic halo (0.05–0.22 mm wide) that produced the white-walled appearance in hand specimen (Fig. 10D). However, haloes are absent from vesicles in the uppermost (upper tens of centimeters) glassy crust.

DISCUSSION

Breakouts represent an important part of the emplacement process and constitute ~12% of the final lava flow volume at Cordón Caulle. Furthermore, evidence from satellite images, field observations (Tuffen et al., 2013), and numerical modeling (Farquharson et al., 2015) indicate that they can remain active, and hence hazardous, many months after effusion ended.

Conditions for Breakout Formation

For breakouts to form, the local conditions must evolve to favor the initiation of a new path for lava advance rather than continuing with the current scenario. Initiation of a breakout arises when flow front advance slows or ceases, despite continued lava supply from the vent, and can result in a change in the direction of lava propagation. More specifically, breakouts form when the internal pressure within the lava flow exceeds the local confining force, due to increased core pressure and/or decreased crust strength. Crust weakening is enhanced by lateral spreading of lava flow front lobes (Applegarth et al., 2010a) and higher effusion rates at the vent can increase core pressure by propagating an increased supply rate to the lava flow front, even if the front is still advancing. Within-flow crystallization (e.g., second boiling) can also pressurize the core by increasing the melt vapor pressure, leading to vesicle growth.

Breakout Initiation

At Cordón Caulle, both internal pressure increase and crustal weakening are likely to have contributed to breakout formation. The breakouts that formed from the completely stalled lava flow margins, in areas without clear crustal weakening (as indicated by crust fractures) such as the static margin of the southern branch (e.g., Figs. 6A and 7), suggest that the

TABLE 2. PROPERTIES OF THE BREAKOUT TYPES (BASED ON MEASUREMENTS OF ~30 BREAKOUTS)

Breakout type	Length (m)*	Width (m)*	Thickness (m)†	Volume (m^3)	Fragment size (m)
Domed	15–80	15–100	15–30	~4×10^3 – ~2×10^5	~5–15
Petaloid	70–230	60–150	25–30	~1×10^5 – ~9×10^5	~5–10
Rubbly	110–2000	120–200	30	~5×10^5 – ~1×10^7	~1–5
Cleft-split	160–340	50–150	30–35	~3×10^5 – ~1×10^6	~1–15

*Measured from Google Earth imagery.
†Measured from Pléiades digital elevation model profiles.

core pressure of the lava exceeded the yield strength of the surface crust, which, based on previous work is likely to be between 10^6 and 10^8 Pa (Griffiths and Fink, 1993; Bridges, 1997; Fink and Griffiths, 1998; DeGroat-Nelson et al., 2001; Magnall et al., 2017). Such pressure increases could have resulted from the continued supply of lava through thermally preferential pathways (or "fluid pathways") beneath the static surface crust. Alternatively, small domed breakouts formed from static portions of the lava flow margins, where thermal pathways were likely absent or potentially only locally developed (Fig. 1), suggest that more local processes, such as margin collapse or late stage core vesiculation, could also have been important.

Late-stage vesiculation occurred within most breakouts, indicated by the presence of a relatively undeformed vesicle population (Figs. 9C, 10, and 11); the limited deformation interpreted to reflect a short distance of flow, e.g., from breakout advance only. Consequently, these vesicles probably result from volatile exsolution either due to a pressure decrease during breakout extrusion, or due to crystallization occurring between the vent and lava flow front. Lava crystallinity increases from <25 vol% at the vent (as low as <5 vol% in some lava-flow-top-pumice samples) to ~30–40 vol% in breakout samples. The increase in crystallinity as lava moved toward breakouts will have increased the volatile concentration in the melt and potentially driven second boiling (Manley and Fink, 1987) or enhanced vesicle nucleation and growth, if the melt was already at volatile saturation. Some support for distal volatile exsolution from the lava flow core is provided by the observations of outgassing plumes at

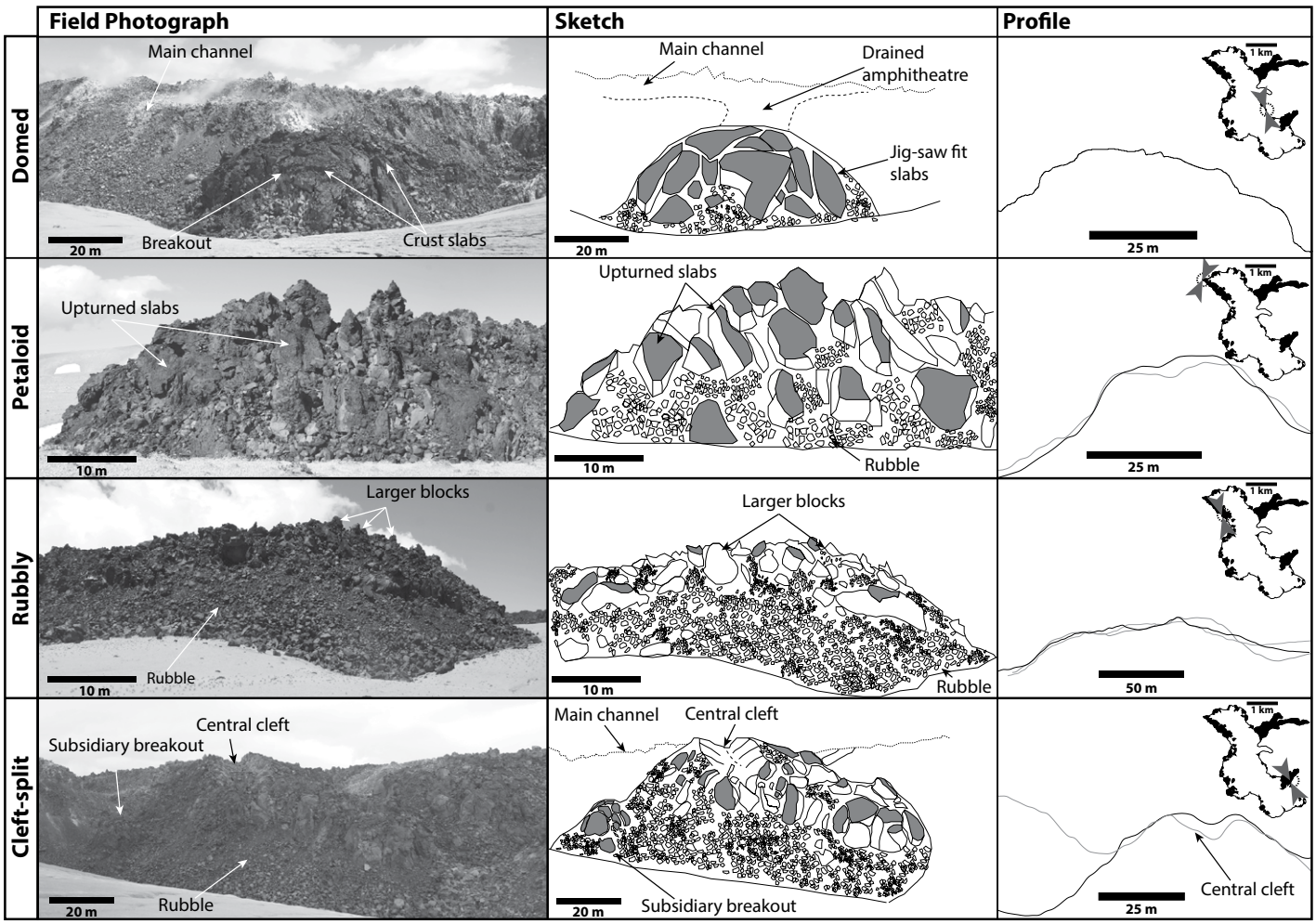

Figure 8. Breakout morphologies, 2-D profiles, and location maps of the breakouts from the 2011–2012 Cordón Caulle lava flow, southern Chile. The breakouts are categorized as domed, petaloid, rubbly, and cleft-split. The profile for the domed breakout derives from a 3-D photogrammetry model (Fig. 7), the others are derived from a Pléiades 1 m digital elevation model (DEM), and the gray profiles are from similar breakout types. The arrows in the sketch maps show the approximate locations of the breakouts and the orientation of the profiles. The clefts can be seen as a dip in the breakout profile, it is worth noting that the true depth of the cleft is unlikely to be resolved by the DEM.

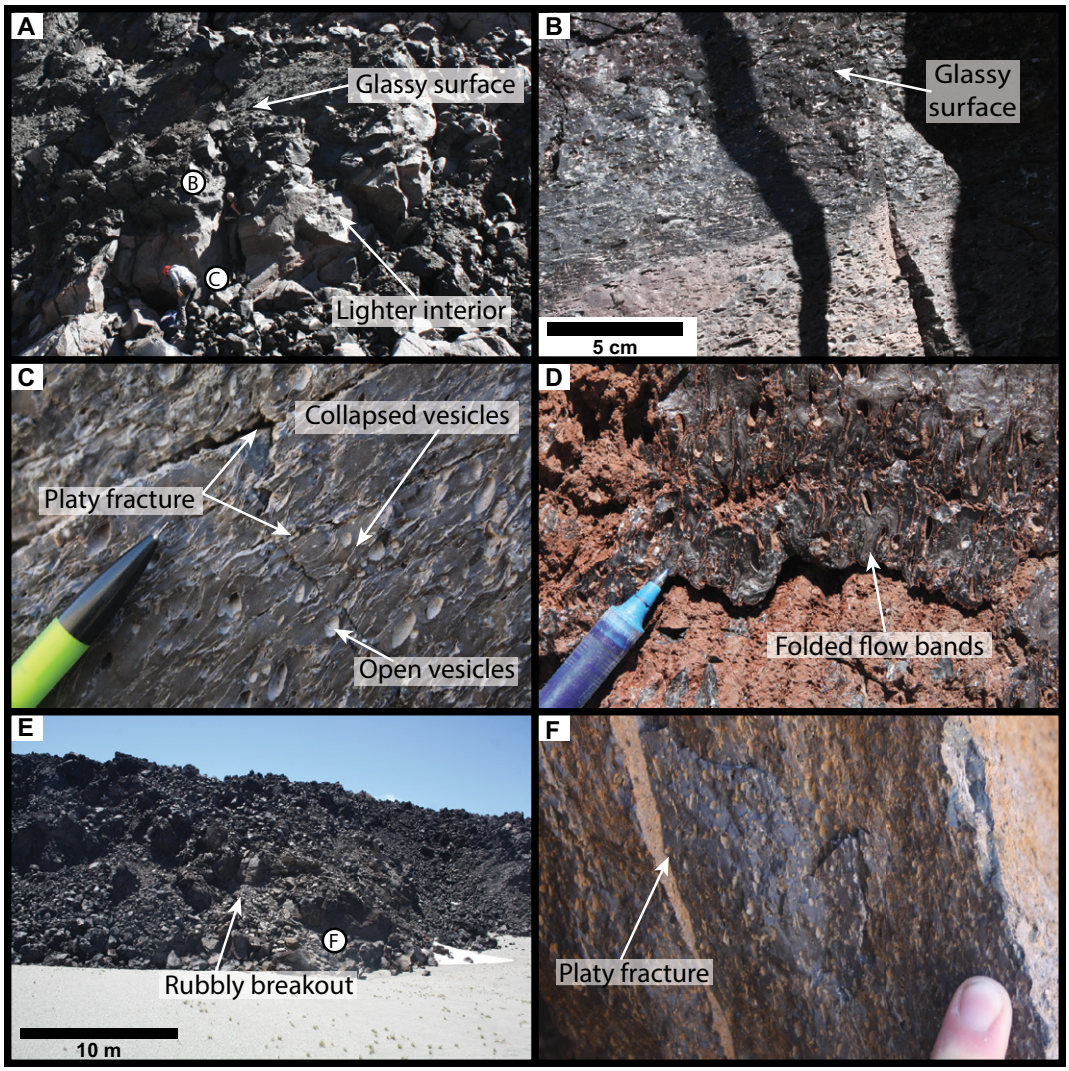

Figure 9. Breakout lava from the 2011–2012 Cordón Caulle lava flow, southern Chile. (A) A surface slab at the front of a breakout; the darker surface is glass whereas the interior is lighter in color. (B) The contact between the glassy surface crust and the lighter lava core. (C) The core of the breakout is lighter and includes a large number of cristobalite-coated vesicles, some of which are deformed or collapsed and others are undeformed and open. (D) Flow-banded breakout lava in a fallen fragment at the lava flow front; the flow-bands are extensively folded. (E) The base of a rubbly breakout; the vesicular rhyolite developed a small number of platy fractures similar to those observed in the crystalline core lava (F).

the stalled lava flow front (Figs. 6C and 12) but, strictly, this is proof only of gas migration and escape, and concurrent vesicle growth for contributing to pressure increase can only be inferred. Nevertheless, this gas remobilization likely contributed to the precipitation of cristobalite throughout the lava flow (Schipper et al., 2015) and late-stage volatile exsolution, driven by in-flow crystallization, has also been inferred to form the vesicular layers observed in many prehistoric rhyolite lavas (e.g., Fink, 1980b; Fink and Manley, 1987; Manley and Fink, 1987).

The large extensional fractures associated with lobe formation at the lava flow front were often preferential regions of breakout formation; breakouts appear to exploit the weakened crust (Figs. 6B and 12B). A similar process has been observed in laboratory experiments, where tensile surface fractures in a spreading and lobate analogue lava flow front enabled upwelling of the viscous core (Applegarth et al., 2010a).

Breakout Evolution

The growth and inflation of breakouts is inferred to have occurred through a combination of continued magma supply and vesiculation. The smaller, morphologically more simple breakouts form from areas of the lava flow without continued supply by thermally preferential pathways (i.e., the lateral margins rather than the fronts; Figs. 1 and 8). Small domed breakouts, some with a drained amphitheater structure in the adjacent levee (Figs. 6A, 12A, and 13D), indicate a limited, local magma supply. In these breakouts, vesiculation caused by decompression after extrusion from the main branches could have played a significant role in the overall inflation, with the observed vesicularities (15–30 vol%, Table 1) representing a potential contribution of meters to inflation (or a lateral advance of tens of meters). Decompression-driven vesiculation of breakout lava likely contributed to the formation of their scoriaceous and glassy crust (Fig. 9) which grades into the lighter, gray, breakout interior with abundant globulites (Fig. 10A). Given that globulites form due to devitrification below the glass transition temperature (Schipper et al., 2015), their growth is unlikely to have driven vesiculation within breakouts and they probably had negligible influence on breakout development.

Breakout inflation causes increased fracturing and upturning of surface slabs (Tuffen et al., 2013). From observations of inflation (Tuffen et al., 2013), intermediate morphologies, and the development of inflationary clefts (Fig. 3), we infer a breakout evolution from domed to petaloid, to rubbly then cleft-split morphologies. Cleft-split morphologies may also develop directly from petaloid breakouts where continued lava supply leads to inflation, rather than advance. The striated surfaces of the resulting clefts mark repeated transitions from brittle fracturing to ductile tearing during the cleft opening (Forbes et al., 2012; Forbes et al., 2014). How-

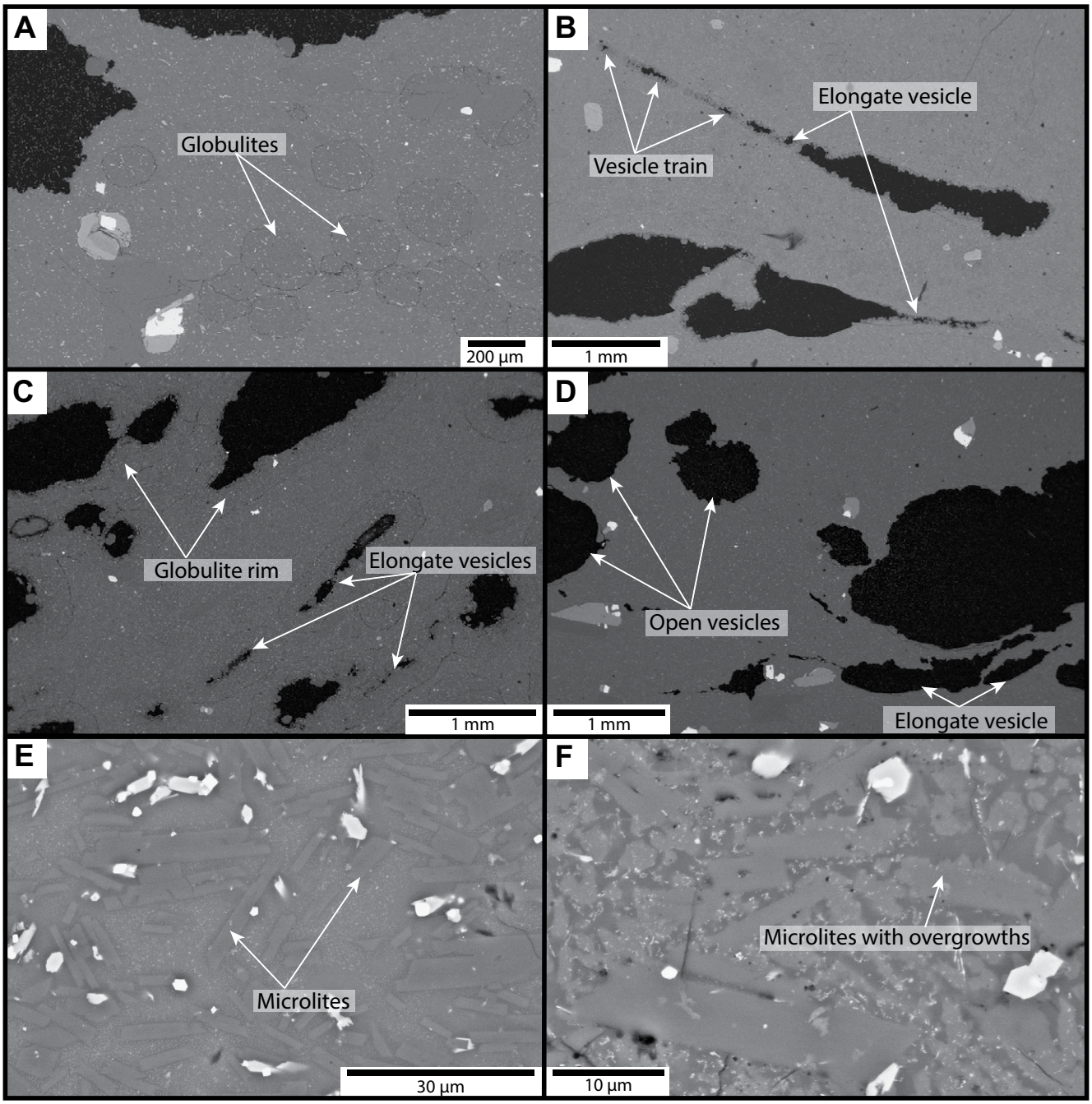

Figure 10. Scanning electron microscopy images of breakout samples from the 2011–2012 Cordón Caulle lava flow, southern Chile. (A) Globulites in glassy rhyolite. (B) Partially collapsed and elongate bubble trains in the glassy surface of a breakout. (C) Sheared vesicles with a rim of globulites surrounding the vesicles. (D) More open and undeformed vesicles from the surface samples of a breakout; the vesicles lack the globulite rims. (E) Typical feldspar microlites in a glassy groundmass of a breakout sample; some of these microlites have growth rims. (F) Feldspar microlites in the globulites have distinctive uneven overgrowths. The globulites are almost entirely crystalline and the space between the crystals is occupied by cristobalite.

ever, clefts do not have the centimeter-scale striations and convex sides typical of crease structures commonly observed at other silicic lavas and domes, which suggests that the simultaneous upwelling and deformation of core lava associated with crease structure formation did not occur (c.f. Anderson and Fink, 1990; Anderson and Fink, 1992). We therefore propose that the formation of clefts within cleft-split breakouts is similar to that of "lava-inflation clefts" observed in basaltic pahoehoe tumuli, where a surface crust is buckled upwards by an increased core pressure (Walker, 1991). Nevertheless, in contrast to basaltic lavas, we consider that late-stage vesiculation at Cordón Caulle provided an important contribution to this inflation.

The sustained advance of breakouts further promoted crust brecciation, and breakouts that

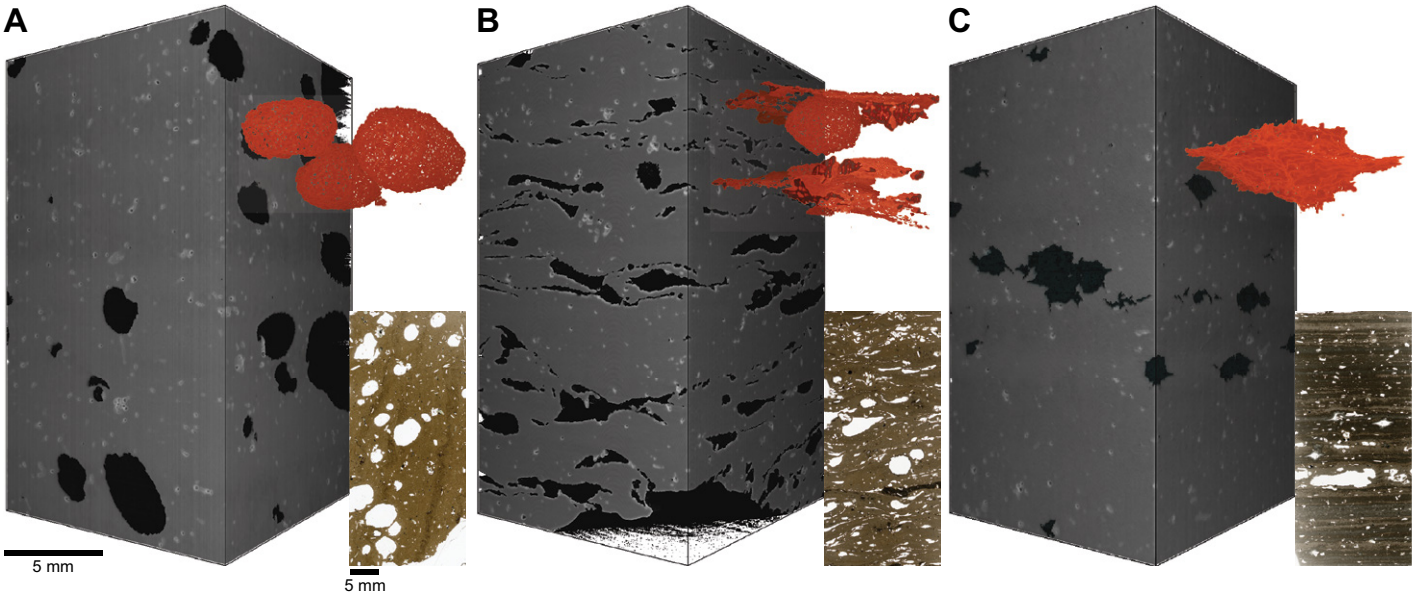

Figure 11. 3-D computed tomography renderings and associated thin section scans of representative breakout samples from the 2011–2012 Cordón Caulle lava flow, southern Chile. For each sample, main volume is rendered by solid lava in gray, with slight transparency to show internal pores within the volume. Red images show expanded view of selected pores. Subjacent frames show standard petrographic thin sections for each sample. (A) Breakout with little indication of shear or compaction, relatively glassy groundmass, and sub-spherical pores. (B) Moderately compacted breakout, with moderately crystalline and flow-banded groundmass. There are sub-spherical vesicles within this sample. (C) Highly compacted and crystallized core of the main lava. Note that despite nearly complete compaction, the sample maintains a few vesicles. The ragged appearance of these surviving vesicles (red pore in C) is not an analytical artifact, but represents the actual roughness of the surviving pores.

were active for months required the establishment of extended thermally preferential pathways to maintain a continued lava supply. In one of the longer rubbly breakouts, the observation of platy fractures suggests that sustained breakouts may begin to develop microstructure characteristics comparable with those of the main branches. With such characteristics not observed in smaller breakouts, it is likely that the presence of platy fractures reflects processes that occur only toward the end of the emplacement of long breakouts or substantial branches.

The surface morphology of a breakout may also reflect the rate at which it grows, just as the transition from pahoehoe to ‘a’ā lava can be driven by increased effusion and strain rates (Pinkerton and Sparks, 1976; Rowland and Walker, 1990; Cashman et al., 1999; Hon, 2003). In analogue experiments of silicic lava dome formation, low effusion rates (relative to cooling rate) aided surface crust formation and favored spiny or platy morphologies (Fink and Griffiths, 1998), whereas higher effusion rates created smoother and lower profiles (Fink and Griffiths, 1998). Thus, we propose that the larger volume rubbly breakouts (Table 2) formed at higher supply rates than domed and petaloid breakouts, with higher supply rates facilitated by efficient thermally preferential pathways. Future work should attempt to systematically relate breakout properties (i.e., volume, effusion rate, rheology) to breakout morphologies and the transitions between different morphological types. Such work would likely combine analysis of breakout types, and comparisons to features generated in analogue experiments (e.g., Griffiths and Fink, 1993; Griffiths and Fink, 1997; Fink and Griffiths, 1998).

Finally, it is likely that breakouts did not all evolve independently, particularly those linked by thermally preferential pathways. For example, the onset of the formation of the large northeast breakout coincided with a decreased rate of new breakout initiation from the main northern lava flow (Fig. 1, Data Repository file 1). This relationship suggests that the supply of lava toward the northeast breakout reduced lava supply to the northern branch. Nevertheless, the drainage (or partial drainage) of thermally preferential pathways enabled continued formation and evolution (e.g., fracture growth) of some breakouts even after effusion at the vent had ceased (Fig. 3). The rubbly northeast breakout ultimately attained a final length of ~2 km and it represents an example of the challenge for hazard forecasting that late-stage breakouts present.

Breakout Formation at Other Lavas

Breakouts are widespread in basaltic lava flow fields where the process of continued flow beneath a static surface crust is a fundamental aspect of the inflation and growth of pahoehoe flow fields (e.g., Self et al., 1996; Anderson et al., 1999; Vye-Brown et al., 2013) and is a recognized process in lengthening ‘a’ā flow fields (e.g., Calvari and Pinkerton, 1998). In both basaltic and silicic lava flows, the continued supply of lava to a stalled lava flow front can generate breakout formation through driving a pressure increase and eventual rupturing of the surface crust (Pinkerton and Sparks, 1976; Blake and Bruno, 2000). However, in silicic lava flows, crystallization-driven late-stage vesiculation or vesicle growth is also likely to provide an important contribution to pressurization. This process will not be as important in basaltic lava flows, where lower lava viscosities allow faster bubble migration (e.g., Vergniolle and Jaupart, 1986) and substantial vesicle loss can be measured with increasing distance from the vent (Cashman et al., 1994). However, vesiculation-driven inflation may play a minor role in the observed inflation of some mafic lava flows and lava lakes (e.g., Peck, 1978; Stevens et al., 2001).

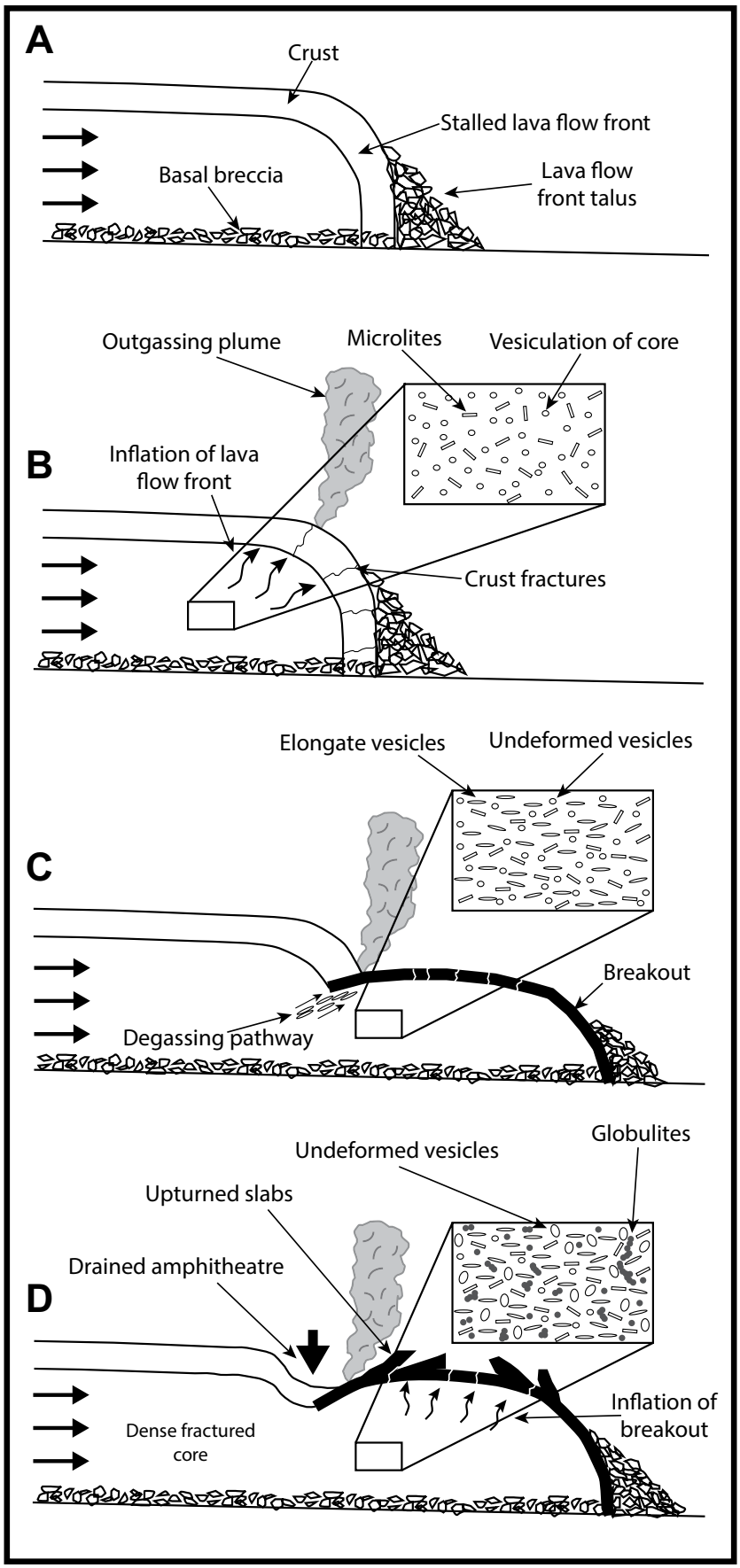

Figure 12. Schematic cross sections of breakout formation at the 2011–2012 Cordón Caulle lava flow, southern Chile. (A) The lava flow stalls due to the strength of the cooled surface crust. (B) Lava continues to be supplied to the lava flow front leading to inflation. Vesiculation of the lava core, partly driven by ongoing anhydrous crystallization, applies pressure to the lava crust, causing it to fracture. (C) The crust fails and a breakout forms. As the breakout extrudes, some vesicles are sheared and partially collapse as volatiles escape from the lava. The drop in pressure during breakout formation leads to further vesiculation of the breakout surface. (D) As the breakout extrudes, sections of the main branch surface drained to form an amphitheater behind the breakout. Continued supply to the breakout, coupled with core vesiculation, leads to inflation and upturning of surface slabs. Globulites formed in the breakout core after emplacement and below the glassy surface crust, these have limited impact on the breakout development.

The prevalence of breakouts in silicic lava flows may be currently underestimated, and other likely candidates are present in an earlier lava at Cordón Caulle (1960). One of the 1960 lavas has a thin lobe (800 m long and 80 m wide, 40.542765°S, 72.235110°W) with an overall morphology similar to the northeast breakout of the 2011–2012 lava (Fig. 1). At the front of this rubbly potential 1960 breakout, a domed and slabby front (~50 m in diameter) resembles a transitional domed-to-petaloid breakout (Fig. 8). In some of the large rhyolite lavas in the western USA, marginal lobes (often interpreted as forming due to the splitting of the lava flow front) have also been identified (Bonnichsen and Kauffman, 1987; Manley, 1992, 1996) but they have not been discussed in terms of breakout processes. The margin of the dacitic portion of Glass Mountain at Medicine Lake Volcano, California, USA, has a particularly pronounced lobate flow front, and satellite images show that some lobe surfaces partially comprise large fractured slabs, similar to the domed and petaloid breakouts at Cordón Caulle (Figs. 8 and 13). Unfortunately, the age of the Glass Mountain lava (several thousand years) makes definitive identification of breakouts challenging in remotely sensed data. Although the Cordón Caulle lava has a similar lobate morphology to the dacitic portion of Big Glass Mountain (61.3–67.3% SiO_2, Donnelly-Nolan et al., 2016), it is substantially different from the rhyolitic portion (70–75% SiO_2,

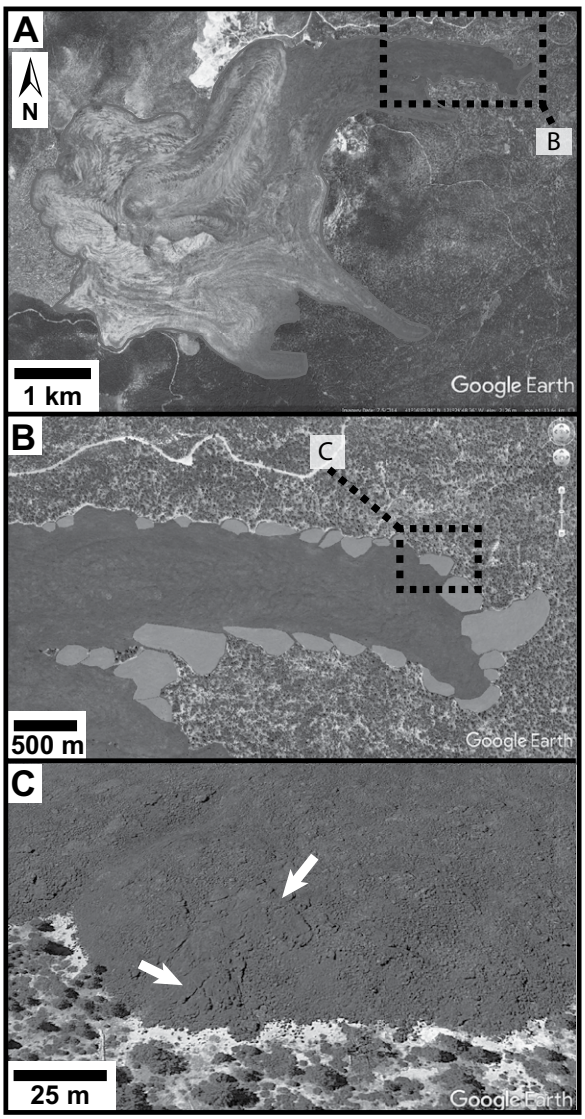

Figure 13. (A) Google Earth image of the Big Glass Mountain Dacite-Rhyolite lava flow (Medicine Lake Volcano, California, USA). (B) Shaded areas show potential breakouts from the dacitic portion of the lava flow. (C) Arrows highlight a slabby and fractured area of the lava flow front that is similar in appearance to the breakouts at the Cordón Caulle lava flow.

Donnelly-Nolan et al., 2016), which lacks such a lobate margin (Fig. 13). This difference could suggest that emplacement processes for the Cordón Caulle lava flow had more in common with those of glassy dacitic lava flows than some higher silica rhyolite lava flows.

Although breakouts are not readily identifiable at most other rhyolite lavas, other emplacement features have been linked to late-stage vesiculation. In some higher silica (>70% SiO_2) rhyolites, diapirs of coarsely vesicular pumice (Fink, 1980b, 1983; Fink and Manley, 1987) are thought to form due to bubble growth in the core of the lava flow (Manley and Fink, 1987; Furukawa and Uno, 2015) and could represent a vertically orientated equivalent of lateral breakouts. Similarly, the formation of large gas cavities capable of triggering small explosions (DeGroat-Nelson et al., 2001; Castro et al., 2002), is thought to be caused by the accumulation of gas, in association with a buckling surface crust, in a layer directly beneath the surface crust (Jensen, 1993; Castro et al., 2002). The late-stage vesiculation inferred at Cordón Caulle did not lead to any observed pumice diapirs or substantial gas cavities, and further work could explore whether the small compositional differences between Cordón Caulle and more silicic rhyolites are responsible for observed differences in late-stage evolution.

CONCLUSIONS

The 2011–2012 rhyolite lava flow at Cordón Caulle generated ~90 breakouts and provided the first observations of breakout processes during such an eruption. Our multi-scale analyses have enabled a morphological classification of rhyolite breakouts and given insight into their importance as part of the emplacement of silicic lava flows. The breakouts are likely initiated by a combination of pressure build-up in the core of the lava flow (due to continued lava supply and vesiculation, partly driven by in-flow crystal growth), and fracturing of the surface crust. During and after extrusion from the slowed lava flow margins the breakouts developed into a sequence of morphologies from domed, petaloid, rubbly, to cleft-split, which reflected their evolving stages of growth and inflation. Inflation is inferred to be driven by both lava supply and vesiculation within the core of a breakout, and was responsible for the breakup of surface slabs and the formation of inflation clefts.

The continued supply and growth of breakouts was due to the presence of active thermally preferential pathways, supplying fresh lava beneath a stationary lava crust after advance of the main flow had ceased. The potential presence of such pathways should be considered in the interpretation of emplacement processes at other laterally extensive rhyolite lavas. Furthermore, the evidence for late-stage vesiculation in breakouts has substantial hazard implications; volatile accumulation could lead to surface explosions or flow front collapse. The processes of breakout formation and lava supply through thermally preferential pathways that we have showed for a rhyolite lava are well-studied in mafic lava flows, and direct comparisons can be made across the compositions. However, in rhyolites, the driving effects of late-stage vesiculation are likely to be strongly enhanced with respect to those in basalts, due to the high-viscosity inhibiting pressure release and vesicle migration.

ACKNOWLEDGEMENTS

NM is supported by a Natural Environment Research Council-Envision studentship and a British Geological Survey University Funding Initiative grant. HT is supported by a Royal Society University Research Fellowship. CV-B publishes with the express permission of the executive director of the British Geological Survey. CIS acknowledges access to the Australian Synchrotron's Imaging and Medical Beamline, Clayton, Victoria, granted under proposals 2014/1-M7574 and 2017/1-M11688, with travel support from the New Zealand Synchrotron Group Ltd. JMC is supported by the Volcanoes and Atmosphere in Magmatic Open Systems research center, University of Mainz, Germany. We gratefully acknowledge the assistance of Gren Turner (British Geological Survey) with scanning electron microscope imaging of the thin sections. We also wish to thank the BBC Earth team for assistance with aerial photography of the lava flow. Earth Observing (EO-1) data were obtained via the National Aeronautics and Space Administration's (NASA) Volcano Sensor Web at the Jet Propulsion Laboratory, California Institute of Technology, Pasadena, California, USA. EO-1 was managed by the NASA Goddard Space Flight Center, Greenbelt, Maryland, USA. We gratefully acknowledge editorial handling and helpful comments from Brad S. Singer and Jocelyn McPhie and constructive reviews from Jonathan Fink and an anonymous reviewer.

REFERENCES CITED

Anderson, S.W., and Fink, J.H., 1990, The Development and Distribution of Surface Textures at the Mount St. Helens Dome, *in* Fink, J.H., ed., Lava Flows and Domes: Emplacement Mechanisms and Hazard Implications: IAVCEI Proceedings of Volcanology, Berlin, Germany, Springer, v. 2, p. 25–46, https://doi.org/10.1007/978-3-642-74379-5_2.

Anderson, S.W., and Fink, J.H., 1992, Crease structures: Indicators of emplacement rates and surface stress regimes of lava flows: Geological Society of America Bulletin, v. 104, no. 5, p. 615–625, https://doi.org/10.1130/0016-7606(1992)104<0615:CSIOER>2.3.CO;2.

Anderson, S.W., Stofan, E.R., Smrekar, S.E., Guest, J.E., and Wood, B., 1999, Pulsed inflation of pahoehoe lava flows: Implications for flood basalt emplacement: Earth and Planetary Science Letters, v. 168, no. 1-2, p. 7–18, https://doi.org/10.1016/S0012-821X(99)00044-8.

Applegarth, L.J., James, M.R., de Vries, B.V., and Pinkerton, H., 2010a, Influence of surface clinker on the crustal structures and dynamics of 'a'ā lava flows: Journal of Geophysical Research, Solid Earth, v. 115, no. B7, https://doi.org/10.1029/2009jb006965.

Applegarth, L.J., Pinkerton, H., James, M.R., and Calvari, S., 2010b, Morphological complexities and hazards during the emplacement of channel-fed 'a'ā lava flow fields: A study of the 2001 lower flow field on Etna: Bulletin of Volcanology, v. 72, no. 6, p. 641–656, https://doi.org/10.1007/s00445-010-0351-1.

Baum, B.A., Krantz, W.B., Fink, J.H., and Dickinson, R.E., 1989, Taylor instability in rhyolite lava flows: Journal of Geophysical Research, Solid Earth, v. 94, no. B5, p. 5815–5828, https://doi.org/10.1029/JB094iB05p05815.

Bernstein, M., Pavez, A., Varley, N., Whelley, P., and Calder, E.S., 2013, Rhyolite lava dome growth styles at Chaiten Volcano, Chile (2008–2009): Interpretation of thermal imagery: Andean Geology, v. 40, no. 2, p. 295–309, https://doi.org/10.5027/andgeoV40n2-a07.

Bertin, D., Lara, L.E., Basualto, D., Amigo, Á., Cardona, C., Franco, L., Gil, F., and Lazo, J., 2015, High effusion rates of the Cordón Caulle 2011–12 eruption (Southern Andes) and their relation with the quasi-harmonic tremor: Geophysical Research Letters, v. 42, no. 17, p. 7054–7063, https://doi.org/10.1002/2015GL064624.

Bignami, C., Corradini, S., Merucci, L., de Michele, M., Raucoules, D., De Astis, G., Stramondo, S., and Piedra, J., 2014, Multisensor Satellite Monitoring of the 2011 Puyehue-Cordon Caulle Eruption: IEEE Journal of Selected Topics in Applied Earth Observations and Remote Sensing, v. 7, no. 7, p. 2786–2796, https://doi.org/10.1109/JSTARS.2014.2320638.

Blake, S., and Bruno, B.C., 2000, Modelling the emplacement of compound lava flows: Earth and Planetary Science Letters, v. 184, no. 1, p. 181–197, https://doi.org/10.1016/S0012-821X(00)00278-8.

Bonnichsen, B., and Kauffman, D.F., 1987, Physical features of rhyolite lava flows in the Snake River Plain volcanic province, southwestern Idaho, *in* Fink, J.H., ed., The Emplacement of Silicic Domes and Lava Flows: Geological Society of America Special Paper 212, p. 119–145, https://doi.org/10.1130/SPE212-p119.

Bridges, N.T., 1997, Ambient effects on basalt and rhyolite lavas under Venusian, subaerial, and subaqueous conditions: Journal of Geophysical Research: Planets (1991–2012), v. 102, no. E4, p. 9243–9255, https://doi.org/10.1029/97JE00390.

Calvari, S., and Pinkerton, H., 1998, Formation of lava tubes and extensive flow field during the 1991–1993 eruption of Mount Etna: Journal of Geophysical Research. Solid Earth, v. 103, no. B11, p. 27291–27301, https://doi.org/10.1029/97JB03388.

Cashman, K.V., Mangan, M.T., and Newman, S., 1994, Surface degassing and modifications to vesicle size distributions in active basalt flows: Journal of Volcanology and Geothermal Research, v. 61, no. 1, p. 45–68, https://doi.org/10.1016/0377-0273(94)00015-8.

Cashman, K.V., Thornber, C., and Kauahikaua, J.P., 1999, Cooling and crystallization of lava in open channels, and the transition of Pahoehoe Lava to 'a'ā: Bulletin of Volcanology, v. 61, no. 5, p. 306–323, https://doi.org/10.1007/s004450050299.

Castro, J., and Cashman, K.V., 1999, Constraints on rheology of obsidian lavas based on mesoscopic folds: Journal of Structural Geology, v. 21, no. 7, p. 807–819, https://doi.org/10.1016/S0191-8141(99)00070-X.

Castro, J., Cashman, K., Joslin, N., and Olmsted, B., 2002, Structural origin of large gas cavities in the Big Obsidian Flow, Newberry Volcano: Journal of Volcanology and Geothermal Research, v. 114, no. 3-4, p. 313–330, https://doi.org/10.1016/S0377-0273(01)00296-7.

Castro, J.M., Schipper, C.I., Mueller, S.P., Militzer, A.S., Amigo, A., Silva Parejas, C., and Jacob, D., 2013, Storage and eruption of near-liquidus rhyolite magma at Cordon Caulle, Chile: Bulletin of Volcanology, v. 75, no. 4, p. 1–17, https://doi.org/10.1007/s00445-013-0702-9.

Coppola, D., Laiolo, M., Franchi, A., Massimetti, F., Cigolini, C., and Lara, L.E., 2017, Measuring effusion rates of obsidian lava flows by means of satellite thermal data: Journal of Volcanology and Geothermal Research, v. 347, p. 82–90, https://doi.org/10.1016/j.jvolgeores.2017.09.003.

Dadd, K.A., 1992, Structures within large volume rhyolite lava flows of the Devonian Comerong Volcanics, southeastern Australia, and the Pleistocene Ngongotaha lava dome, New Zealand: Journal of Volcanology and Geothermal Research, v. 54, no. 1-2, p. 33–51, https://doi.org/10.1016/0377-0273(92)90113-R.

DeGroat-Nelson, P.J., Cameron, B.I., Fink, J.H., and Holloway, J.R., 2001, Hydrogen isotope analysis of rehydrated silicic lavas: Implications for eruption mechanisms: Earth and Planetary Science Letters, v. 185, no. 3-4, p. 331–341, https://doi.org/10.1016/S0012-821X(00)00379-4.

Digenis, C.J., Lencioni, D.E., and Bicknell, W.E., 1998, New Millennium EO-1 Advanced Land Imager, *in* Proceedings Volume 3439 SPIE Conference on Earth Observing Systems III: San Diego, California, USA, SPIE's International Symposium of Optical Science, Engineering, and Instrumentation, p. 49–55, https://doi.org/10.1117/12.325668.

DigitalGlobe, 2012, WorldView-2 Pan_MS1_MS2 scene 103001001234BC00, 10/04/2012: Accessed from Google Earth.

DigitalGlobe, 2015, WorldView-2 Pan_MS1_MS2 scene 103001003D539F00, 27/02/2015: Accessed from Google Earth.

Donnelly-Nolan, J.M., Champion, D.E., and Grove, T.L., 2016, Late Holocene volcanism at Medicine Lake Volcano, northern California Cascades: U.S. Geological Survey Professional Paper 1822, 59 p., https://dx.doi.org/10.3133/pp1822.

Farquharson, J.I., James, M.R., and Tuffen, H., 2015, Examining rhyolite lava flow dynamics through photo-based 3D reconstructions of the 2011–2012 lava flowfield at Cordón-Caulle, Chile: Journal of Volcanology and Geothermal Research, v. 304, p. 336–348, https://doi.org/10.1016/j.jvolgeores.2015.09.004.

Fierstein, J., and Hildreth, W., 1992, The plinian eruptions of 1912 at Novarupta, Katmai National Park, Alaska: Bulletin of Volcanology, v. 54, no. 8, p. 646–684, https://doi.org/10.1007/BF00430778.

Fink, J., 1980a, Surface folding and viscosity of rhyolite flows: Geology, v. 8, no. 5, p. 250–254, https://doi.org/10.1130/0091-7613(1980)8<250:SFAVOR>2.0.CO;2.

Fink, J.H., 1980b, Gravity instability in the Holocene Big and Little Glass Mountain rhyolitic obsidian flows, northern California: Tectonophysics, v. 66, no. 1-3, p. 147–166, https://doi.org/10.1016/0040-1951(80)90043-8.

Fink, J.H., 1983, Structure and emplacement of a rhyolitic obsidian flow: Little Glass Mountain, Medicine Lake Highland, northern California: Geological Society of America Bulletin, v. 94, no. 3, p. 362–380, https://doi.org/10.1130/0016-7606(1983)94<362:SAEOAR>2.0.CO;2.

Fink, J.H., 1993, The emplacement of silicic lava flows and associated hazards, *in* Kilburn, C.R.J., and Luongo, G., eds., Active Lavas: Monitoring and Modelling: London, UK, UCL Press, p. 5–21.

Fink, J.H., and Griffiths, R.W., 1998, Morphology, eruption rates, and rheology of lava domes: Insights from laboratory models: Journal of Geophysical Research. Solid Earth, v. 103, no. B1, p. 527–545, https://doi.org/10.1029/97JB02838.

Fink, J.H., and Kieffer, S.W., 1993, Estimate of pyroclastic flow velocities resulting from explosive decompression of lava domes: Nature, v. 363, p. 612–615, https://doi.org/10.1038/363612a0.

Fink, J.H., and Manley, C.R., 1987, Origin of pumiceous and glassy textures in rhyolite flows and domes, *in* Fink, J.H., ed., The Emplacement of Silicic Domes and Lava Flows: Geological Society of America Special Paper 212, p. 77–88, https://doi.org/10.1130/SPE212-p77.

Forbes, A.E.S., Blake, S., McGarvie, D.W., and Tuffen, H., 2012, Pseudopillow fracture systems in lavas: Insights into cooling mechanisms and environments from lava flow fractures: Journal of Volcanology and Geothermal Research, v. 245, p. 68–80, https://doi.org/10.1016/j.jvolgeores.2012.07.007.

Forbes, A.E.S., Blake, S., Tuffen, H., and Wilson, A., 2014, Fractures in a trachyandesitic lava at Öræfajökull, Iceland, used to infer subglacial emplacement in 1727–8 eruption: Journal of Volcanology and Geothermal Research, v. 288, no. 0, p. 8–18, https://doi.org/10.1016/j.jvolgeores.2014.10.004.

Furukawa, K., and Uno, K., 2015, Origin and deformation of high porosity bands in the Takanoobane Rhyolite lava of Aso volcano, Japan: Journal of Volcanology and Geothermal Research, v. 305, p. 76–83, https://doi.org/10.1016/j.jvolgeores.2015.09.021.

Global Volcanism Program, 2012, Report on Puyehue-Cordón Caulle (Chile), *in* Sennert, S.K., ed., Weekly Volcanic Activity Report, 18 April–24 April 2012: Smithsonian Institution and US Geological Survey.

Griffiths, R.W., and Fink, J.H., 1993, Effects of surface cooling on the spreading of lava flows and domes: Journal of Fluid Mechanics, v. 252, p. 667–702, https://doi.org/10.1017/S0022112093003933.

Griffiths, R.W., and Fink, J.H., 1997, Solidifying Bingham extrusions: A model for the growth of silicic lava domes: Journal of Fluid Mechanics, v. 347, p. 13–36, https://doi.org/10.1017/S0022112097006344.

Harris, A.J.L., and Flynn, L.P., 2002, The thermal stealth flows of Santiaguito dome, Guatemala: Implications for the cooling and emplacement of dacitic block-lava flows: Geological Society of America Bulletin, v. 114, no. 5, p. 533–546, https://doi.org/10.1130/0016-7606(2002)114<0533:TTSFOS>2.0.CO;2.

Harris, A.J.L., Flynn, L.P., Matias, O., Rose, W.I., and Cornejo, J., 2004, The evolution of an active silicic lava flow field: An ETM+ perspective: Journal of Volcanology and Geothermal Research, v. 135, no. 1-2, p. 147–168, https://doi.org/10.1016/j.jvolgeores.2003.12.011.

Higgins, M.D., 2000, Measurement of crystal size distributions: The American Mineralogist, v. 85, no. 9, p. 1105–1116, https://doi.org/10.2138/am-2000-8-901.

Higgins, M.D., 2002, Closure in crystal size distributions (CSD), verification of CSD calculations, and the significance of CSD fans: The American Mineralogist, v. 87, no. 1, p. 171–175, https://doi.org/10.2138/am-2002-0118.

Hon, K., 2003, The transition from 'A'ā to Pāhoehoe crust on flows emplaced during the Pu'u 'Ō'ō-Kūpaianaha eruption: U.S. Geological Survey Professional Paper, v. 1676, p. 89–103.

James, M.R., and Robson, S., 2012, Straightforward reconstruction of 3D surfaces and topography with a camera: Accuracy and geoscience application: Journal of Geophysical Research, Earth Surface, v. 117, no. F3, p. 1–17, https://doi.org/10.1029/2011JF002289.

Jensen, R.A., 1993, Explosion craters and giant gas bubbles on Holocene rhyolite flows at Newberry Crater, Oregon: Oregon Geology, v. 55, no. 1, p. 13–19.

Katsui, Y., and Katz, H.R., 1967, Lateral fissure eruptions in the southern Andes of Chile: Journal of the Faculty of Science, Hokkaido University, Series 4, Geology and Mineralogy, v. 13, no. 4, p. 433–448.

Kilburn, C.R.J., and Lopes, R.M.C., 1988, The growth of AA lava flow fields on Mount Etna, Sicily: Journal of Geophysical Research, Solid Earth, v. 93,

no. B12, p. 14759–14772, https://doi.org/10.1029/JB093iB12p14759.

Lara, L.E., Naranjo, J.A., and Moreno, H., 2004, Rhyodacitic fissure eruption in Southern Andes (Cordón Caulle; 40.5°S) after the 1960 (Mw:9.5) Chilean earthquake: A structural interpretation: Journal of Volcanology and Geothermal Research, v. 138, no. 1-2, p. 127–138, https://doi.org/10.1016/j.jvolgeores.2004.06.009.

Limaye, A., 2012, Drishti: A volume exploration and presentation tool, *in* Proceedings Volume 8506, Developments in X-Ray Tomography VIII, 85060X: San Diego, California, USA, SPIE Optical Engineering and Applications, https://doi.org/10.1117/12.935640.

Lofgren, G., 1971, Experimentally produced devitrification textures in natural rhyolitic glass: Geological Society of America Bulletin, v. 82, no. 1, p. 111–124, https://doi.org/10.1130/0016-7606(1971)82[111:EPDTIN]2.0.CO;2.

Magnall, N., James, M.R., Tuffen, H., and Vye-Brown, C., 2017, Emplacing a Cooling-Limited Rhyolite Lava Flow: Similarities with Basaltic Lava Flows: Frontiers of Earth Science, v. 5, no. 44, https://doi.org/10.3389/feart.2017.00044.

Manley, C.R., 1992, Extended cooling and viscous flow of large, hot rhyolite lavas: Implications of numerical modeling results: Journal of Volcanology and Geothermal Research, v. 53, no. 1-4, p. 27–46, https://doi.org/10.1016/0377-0273(92)90072-L.

Manley, C.R., 1996, Physical volcanology of a voluminous rhyolite lava flow: The Badlands lava, Owyhee plateau, southwestern Idaho: Journal of Volcanology and Geothermal Research, v. 71, no. 2-4, p. 129–153, https://doi.org/10.1016/0377-0273(95)00066-6.

Manley, C.R., and Fink, J.H., 1987, Internal textures of rhyolite flows as revealed by research drilling: Geology, v. 15, no. 6, p. 549–552, https://doi.org/10.1130/0091-7613(1987)15<549:ITORFA>2.0.CO;2.

NASA, 2011a, EO-1 ALI scene EO1A2330882011212110KF_1T: Image Courtesy of U.S. Geological Survey, 31/07/2011.

NASA, 2011b, EO-1 ALI scene EO1A2330882011308110KF_1T: Image Courtesy of U.S. Geological Survey, 04/11/2011.

NASA, 2011c, EO-1 ALI scene EO1A2330882011282110KF_1T: Image Courtesy of U.S. Geological Survey, 09/10/2011.

NASA, 2011d, EO-1 ALI scene EO1A2330882011357110PF_1T: Image Courtesy of U.S. Geological Survey, 23/12/2011.

NASA, 2011e, Landsat 5 TM scene LT52330882011177COA00: Image Courtesy of U.S. Geological Survey, 26/06/2011.

NASA, 2012, EO-1 ALI scene EO1A2330882012026110KF_1T: Image Courtesy of U.S. Geological Survey, 26/01/2012.

NASA, 2013, EO-1 ALI scene EO1A2330882013013110PF_1T: Image Courtesy of U.S. Geological Survey, 13/01/2013.

NASA/METI, 2011a, ASTER scene AST_L1T_00310242011145240_20150608034435: Image courtesy of the NASA Land Processes Distributed Active Archive Center (LP DAAC), USGS Earth Resources Observation and Science (EROS) Center, 24/10/2011, https://doi.org/10.5067/ASTER/AST_L1T.003.

NASA/METI, 2011b, ASTER scene AST_L1T_00312272011145305_20150608212959: Image courtesy of the NASA Land Processes Distributed Active Archive Center (LP DAAC), USGS Earth Resources Observation and Science (EROS) Center, 27/12/2011, https://doi.org/10.5067/ASTER/AST_L1T.003.

NASA/METI, 2012, ASTER scene AST_L1T_00302132012145257_20150609123045: Image courtesy of the NASA Land Processes Distributed Active Archive Center (LP DAAC), USGS Earth Resources Observation and Science (EROS) Center, 13/02/2012, https://doi.org/10.5067/ASTER/AST_L1T.003.

Peck, D.L., 1978, Cooling and vesiculation of Alae Lava Lake, Hawaii: U.S. Geological Survey Professional Paper 935-B, 59 p.

Pinkerton, H., and Sparks, R.S.J., 1976, The 1975 subterminal lavas, Mount Etna: Case history of formation of a compound lava field: Journal of Volcanology and Geothermal Research, v. 1, no. 2, p. 167–182, https://doi.org/10.1016/0377-0273(76)90005-6.

Reynolds, M.A., Best, J., and Johnson, R.W., 1980, 1953–57 Eruption of Tuluman Volcano: Rhyolitic Volcanic Activity in the Northern Bismarck Sea: Geological Survey of Papua New Guinea.

Rowland, S.K., and Walker, G.P.L., 1990, Pahoehoe and aa in Hawaii: Volumetric flow rate controls the lava structure: Bulletin of Volcanology, v. 52, no. 8, p. 615–628, https://doi.org/10.1007/BF00301212.

Schipper, C.I., Castro, J.M., Tuffen, H., James, M.R., and How, P., 2013, Shallow vent architecture during hybrid explosive-effusive activity at Cordon Caulle (Chile, 2011–12): Evidence from direct observations and pyroclast textures: Journal of Volcanology and Geothermal Research, v. 262, p. 25–37, https://doi.org/10.1016/j.jvolgeores.2013.06.005.

Schipper, C.I., Castro, J., Tuffen, H., Wadsworth, F., Chappell, D., Pantoja, A., Simpson, M., and Le Ru, E., 2015, Cristobalite in the 2011–2012 Cordón Caulle eruption (Chile): Bulletin of Volcanology, v. 77, no. 5, p. 1–19, https://doi.org/10.1007/s00445-015-0925-z.

Schipper, C.I., Mandon, C., Maksimenko, A., Castro, J.M., Conway, C.E., Hauer, P., Kirilova, M., and Kilgour, G., 2017, Vapor-phase cristobalite as a durable indicator of magmatic pore structure and halogen degassing: An example from White Island volcano (New Zealand): Bulletin of Volcanology, v. 79, no. 10, 74 p., https://doi.org/10.1007/s00445-017-1157-1.

Schneider, C.A., Rasband, W.S., and Eliceiri, K.W., 2012, NIH Image to ImageJ: 25 years of image analysis: Nature Methods, v. 9, no. 7, p. 671–675, https://doi.org/10.1038/nmeth.2089.

Self, S., Thordarson, T., Keszthelyi, L., Walker, G.P.L., Hon, K., Murphy, M.T., Long, P., and Finnemore, S., 1996, A new model for the emplacement of Columbia River basalts as large, inflated pahoehoe lava flow fields: Geophysical Research Letters, v. 23, no. 19, p. 2689–2692, https://doi.org/10.1029/96GL02450.

SERNAGEOMIN/OVDAS, 2012, Puyehue-Cordón Caulle: Reporte especial de actividad volcánica No 331. https://sernageomin.cl/reportesVolcanes/20120316115044320REAV_N331_Los-Rios_Los-Lagos_16032012.pdf.

Singer, B.S., Jicha, B.R., Harper, M.A., Naranjo, J.A., Lara, L.E., and Moreno-Roa, H., 2008, Eruptive history, geochronology, and magmatic evolution of the Puyehue-Cordon Caulle volcanic complex, Chile: Geological Society of America Bulletin, v. 120, no. 5-6, p. 599–618, https://doi.org/10.1130/B26276.1.

Smith, J.V., and Houston, E.C., 1995, Structure of lava flows of the Nimbin Rhyolite, northeast New South Wales: Australian Journal of Earth Sciences, v. 42, no. 1, p. 69–74, https://doi.org/10.1080/08120099508728179.

Stevens, N.F., Wadge, G., Williams, C.A., Morley, J.G., Muller, J.P., Murray, J.B., and Upton, M., 2001, Surface movements of emplaced lava flows measured by synthetic aperture radar interferometry: Journal of Geophysical Research, Solid Earth, v. 106, no. B6, p. 11293–11313, https://doi.org/10.1029/2000JB900425.

Stevenson, R.J., Briggs, R.M., and Hodder, A.P.W., 1994a, Physical volcanology and emplacement history of the Ben Lomond rhyolite lava flow, Taupo Volcanic Center, New-Zealand: New Zealand Journal of Geology and Geophysics, v. 37, no. 3, p. 345–358, https://doi.org/10.1080/00288306.1994.9514625.

Stevenson, R.J., Hodder, A.P.W., and Briggs, R.M., 1994b, Rheological estimates of rhyolite lava flows from the Okataina volcanic center, New-Zealand: New Zealand Journal of Geology and Geophysics, v. 37, no. 2, p. 211–221, https://doi.org/10.1080/00288306.1994.9514616.

Tuffen, H., James, M.R., Castro, J.M., and Schipper, C.I., 2013, Exceptional mobility of an advancing rhyolitic obsidian flow at Cordón Caulle volcano in Chile: Nature Communications, v. 4, https://doi.org/10.1038/ncomms3709.

Vergniolle, S., and Jaupart, C., 1986, Separated two-phase flow and basaltic eruptions: Journal of Geophysical Research, Solid Earth, v. 91, no. B12, p. 12842–12860, https://doi.org/10.1029/JB091iB12p12842.

Vye-Brown, C., Self, S., and Barry, T.L., 2013, Architecture and emplacement of flood basalt flow fields: Case studies from the Columbia River Basalt Group, NW USA: Bulletin of Volcanology, v. 75, no. 3, p. 1–21, https://doi.org/10.1007/s00445-013-0697-2.

Walker, G.P.L., 1971, Compound and simple lava flows and flood basalts: Bulletin Volcanologique, v. 35, no. 3, p. 579–590, https://doi.org/10.1007/BF02596829.

Walker, G.P.L., 1991, Structure, and origin by injection of lava under surface crust, of tumuli, "lava rises", "lava-rise pits", and "lava-inflation clefts" in Hawaii: Bulletin of Volcanology, v. 53, no. 7, p. 546–558, https://doi.org/10.1007/BF00298155.

Yamaguchi, Y., Kahle, A.B., Tsu, H., Kawakami, T., and Pniel, M., 1998, Overview of advanced spaceborne thermal emission and reflection radiometer (ASTER): IEEE Transactions on Geoscience and Remote Sensing, v. 36, no. 4, p. 1062–1071, https://doi.org/10.1109/36.700991.

Science Editor: Bradley S. Singer
Associate Editor: Jocelyn McPhie

Manuscript Received 19 September 2017
Revised Manuscript Received 30 May 2018
Manuscript Accepted 22 June 2018

Printed in the USA